Pyritic mineralization halo above the Tara Deep Zn-Pb deposit, Navan, Ireland: Evidence for sub-seafloor exhalative hydrothermal processes?

**Lola Yesares [1,2], Julian F. Menuge [1], Robert J. Blakeman [3],
John H. Ashton [3], Adrian J. Boyce [4], David Coller [3],
Drew A. Drummond [4] & Ian Farrelly [3]**

[1] *iCRAG and School of Earth Sciences, University College Dublin, Belfield, Dublin 4, Ireland*

[2] *Department of Mineralogy and Petrology, Complutense University of Madrid, Av. Complutense s/n, 28040 Madrid, Spain*

[3] *Boliden Tara Mines DAC, Navan, Co. Meath, Navan, Ireland*

[4] *Scottish Universities Environmental Research Centre, East Kilbride, Glasgow G75 0QF, UK*

Corresponding Author: Lola Yesares   myesares@ucm.es

In Memory of Dr. Robert J. Blakeman who passed on 9th May 2023 for his contribution to this paper and to his work on the understanding of the geology of the Navan deposit - with fond memories from his friends and colleagues.

Pyritic mineralization halo above the Tara Deep Zn-Pb deposit, Navan, Ireland: Evidence for sub-seafloor exhalative hydrothermal processes?

Lola Yesares [1,2], Julian F. Menuge [1], Robert J. Blakeman [3],

John H. Ashton [3], Adrian J. Boyce [4], David Coller [3],

Drew A. Drummond [4] & Ian Farrelly [3]

[1] *iCRAG and School of Earth Sciences, University College Dublin, Belfield, Dublin 4, Ireland*

[2] *Department of Mineralogy and Petrology, Complutense University of Madrid, Av. Complutense s/n, 28040 Madrid, Spain*

[3] *Boliden Tara Mines DAC, Navan, Co. Meath, Navan, Ireland*

[4] *Scottish Universities Environmental Research Centre, East Kilbride, Glasgow G75 0QF, UK*

Abstract: The Tara Deep Zn-Pb deposit, at Navan, Ireland, includes sub-economic pyrite-rich mineralization extending laterally for about 2×2 km within the overlying Lower Visean calc-turbidites, known as the 'New-Thin Bedded Unit'. Here, we investigate the genesis of this pyritic mineralization and its links to the limestone-hosted Zn-Pb deposit lying 100 m below it.

Four mineral assemblages have been identified: 1) in black shales, laminated pyrite comprises thin framboid-rich layers with minor interstitial sphalerite, both showing variable but low δ^{34}S values ranging from -37.4 to 3.3‰; 2) in calcarenite and calcsiltite layers, pyritized fossils are widely distributed and occur chiefly as biodebris replaced by low δ^{34}S pyrite (mean values of -13.2‰); 3) a replacive assemblage occurs as late remobilizations exhibiting both crosscutting and bedding-parallel styles, overprinting the early laminated pyrite. It comprises mostly of marcasite, with minor pyrite, sphalerite, chalcopyrite, galena, stibnite and Co-pentlandite, with high δ^{34}S values up to 24.5‰; and 4) in black shales, bedded sulphide-rich cherts comprising microcrystalline quartz lenses exhibit δ^{18}O mean values of 25.3‰. Cherts are rimmed by dolomite, associated with marcasite, pyrite, sphalerite, chalcopyrite, galena, siegenite and stibnite also with high δ^{34}S values up to 44.2‰. In general terms, pyrite shows a relatively high Co/Ni ratio > 1 and sphalerite Zn/Cd ratios vary from 268 to 364.

Textural analysis indicates overlapping of early-diagenetic and multi-phase hydrothermal sulphide mineralization. Development of laminated pyrite and pyritized calcarenites suggests that this mineralization was generated during early diagenesis, close to the seawater-sediment interface in oxygen-poor conditions under the influence of low-temperature hydrothermal fluid circulation. Later hydrothermal cherts and replacive sulphides suggest discharge of relatively warm hydrothermal fluids during early to mid-diagenesis, presumed to be linked to movements of nearby normal faults. Similarities in mineralogy and S isotope compositions suggest genetic links between the sub-economic pyritic mineralization and the underlying Tara Deep deposit, and consequently, that the former represents a geochemical halo with direct applicability in exploration for Zn-Pb deposits.

Keywords: Subseafloor exhalative replacement, Irish-type deposits, Pyritic halo, Vector tool.

Introduction

Sedimentary exhalative (SedEx) deposits supply >25% of the world's Zn and Pb production (Emsbo, 2009), e.g., the Australian McArthur River (HYC), (Large *et al.*, 2005), and Mt Isa (Rieger et al., 2020), with other major deposits including the Selwyn Basin, Yukon (Gadd *et al.*, 2015; Magnall *et al.*, 2016).

SedEx deposits are hosted mainly by clastic sedimentary rocks (Leach *et al.*, 2005), and form close to the seawater-sediment interface (SWI), in oxygen deficient and organic matter-rich environments (Slack *et al.*, 2004; S´aez *et al.*, 2011). SedEx deposits are formed from oxidized, H_2S-poor and metal-bearing brines generated in hydrothermal reservoirs (Goodfellow & Lydon, 2007). Hydrothermal discharge to the sub-seafloor

occurs via extensional faults, leading to precipitation of *syn-sedimentary* and/or early diagenetic stratiform, stratabound or discordant orebodies (Leach *et al.*, 2010). Bacterial sulphate reduction (BSR) may be the main reduced sulphur source (Goodfellow, 1987; Magnall *et al.*, 2016). In this SedEx model, Pb and Zn sulphide precipitation occurs when bacterially produced H_2S, diffusing upward from anoxic sediment, reacts with Pb-Zn-bearing chloride complexes in the ore-forming fluid (Large *et al.*, 2002; Goodfellow & Lydon, 2007).

SedEx systems are typically long-lived, mostly focused at discrete vent sites in, or at least linked somehow to, faults (Large *et al.*, 2002; Goodfellow & Lydon, 2007). Furthermore, hydrothermal activity commonly continues after sulphide formation, producing widespread post-ore alteration halos extending for hundreds of metres into the stratigraphic hanging-wall sequence and up to several kilometres laterally from the deposit (Goodfellow & Lydon, 2007). Examples include those reported from the Sullivan deposit (Hamilton *et al.*, 1982), Howards Pass in the Yukon (Goodfellow, 2004), Tom (Large, 1981), and Meggen (Gwosdz & Krebs, 1977).

These later and more dispersed hydrothermal products have been used to constrain sources of metals, fluid pathways and mixing sites as well as acting as a vectoring tool (Gregory *et al.*, 2015; Mukherjee & Large, 2017). Fluid-mobile elements can form halos that are much broader than the primary mineralization footprint. In SedEx systems several fluid-mobile elements have been proposed as vectors to aid exploration. For example, in the McArthur River deposit, a widespread Zn, Pb, and Tl halo hosted by pyritic black shale has been described (Large *et al.*, 2000). In addition, a global database constrains metal sources and environmental conditions of sedimentary/diagenetic black shale pyrite formation (Gregory *et al.*, 2015; Large *et al.*, 2017).

Notwithstanding their metallogenetic and potential economic importance, SedEx-related halos are poorly understood. For example, lithological and stratigraphic controls on halo distribution, both regionally and in each deposit, are unclear. Detailed pathways for metal-bearing fluids (e.g., faults, sediment porosity), and SedEx traps are often unknown. The variation of redox conditions in the sedimentary/diagenetic environment as a control on sulphide deposition is also uncertain. The Navan deposit is the largest known Irish-type deposit in the Irish Midlands but also locally includes sub-economic halos, hosted by the overlying Thin Bedded Unit (Ford, 1996; Ashton *et al.*, 2003; Ashton *et al.*, 2015). These halos share many features with classic SedEx deposits, including carbonaceous and clastic host rocks (Hitzman *et al.*, 2002; Ashton *et al.*, 2015) and laminated sulphides parallel to bedding (Ashton *et al.*, 2018).

The most recent potentially economic discovery in the Navan area is the new Irish-type deposit known as Tara Deep, located ~2 km south of the Navan deposit (Fig. 1). With an inferred resource of 26.2 Mt grading 8.4% Zn and 1.6% Pb (Boliden Summary Report Mineral Resources and Mineral Reserves, 2020 Boliden Website), Tara Deep is mainly composed of sphalerite- and galena-rich stratabound lenses hosted by Tournaisian micritic limestones (Fig. 2). The whole Navan Irish-

type system is unconformably overlain by the Fingal Group, a Visean deep marine succession (see Fig. 2 and Ashton *et al.*, 2018). In the Tara Deep area, the Lower Visean succession includes the New-Thin Bedded Unit (N-TBU), which comprises alternating sequences of black shales, siltstones and calcarenites (Figs. 2 and 3) (Yesares *et al.*, 2019). Within this unit, a broad geochemical dispersion halo has been identified showing a spatial link to the underlying micrite-hosted mineralization.

This work focuses on the genesis of the halo above the Tara Deep deposit. We describe the geology, mineralogy, mineral chemistry, in-situ S isotopes and O isotopes hosted by sulphide-rich cherts. These data are then evaluated in order to enhance understanding of how fossil hydrothermal systems operated, in terms of mineralizing fluid evolution, metal mobility and concentration mechanisms. This study serves to strengthen genetic models of both replacive and SedEx mineralization and the possible genetic links between them. It also establishes robust criteria through which geochemical halos of major Irish-type deposits can be identified and used for mineral exploration.

Geological setting

The Irish Midlands basement is dominated by a structurally complex package of Lower Palaeozoic sedimentary and igneous rocks. In the northeast midlands the Ordovician succession comprises shales, sandstones, tuffs, lavas, intrusives and conglomerates (Romano, 1980; Vaughan & Johnston, 1992) and is overlain by Silurian greywackes, sandstones, siltstones, and mud rocks (Vaughan, 1991). These Lower Palaeozoic rocks were deformed and metamorphosed during the closure of the Iapetus Ocean during the Caledonian orogeny (Derry *et al.*, 1965; Leeder, 1982) and are interpreted as having been deposited on the microcontinent of East Avalonia (Fritschle *et al.*, 2018).

The basement is unconformably overlain by the Lower Carboniferous succession which resulted from a south to north marine transgression associated with sedimentary basin development during crustal extension (Philcox, 1984; Phillips & Sevastopulo, 1986; Andrew, 1993; Strogen *et al.,* 1996). The stratigraphy of the Lower Carboniferous of the area begins with the Navan Group, which represents a deepening depositional environment (Philcox, 1984; Philcox, 1989). Its lowermost beds comprise alluvial/marginal marine clastic rocks of Tournaisian age, locally known as Red Beds (Philcox, 1984). These are succeeded by thick, shallow-water, marine carbonates, termed the Laminated Beds, Muddy Limestones and Pale Beds, and comprise mudstones, bioclastic and oolitic grainstones, sandy calcarenites and micrites (Andrew & Ashton, 1985; Anderson, 1990; Rizzi, 1993). These are succeeded by the uppermost rocks of the Navan Group, the Shaley Pales, which comprise shaley bioclastic calcarenites, calcsiltites, shales and sandstones. The Navan Group is overlain by the Cruicetown Group (Rees, 1992), which includes the Argillaceous Bioclastic Limestone (ABL) (Philcox, 1984) and overlying Waulsortian Mudbank Limestone, comprising pale grey micrites, wackestones and packestones (Strogen *et al.*, 1990) (Fig. 2a).
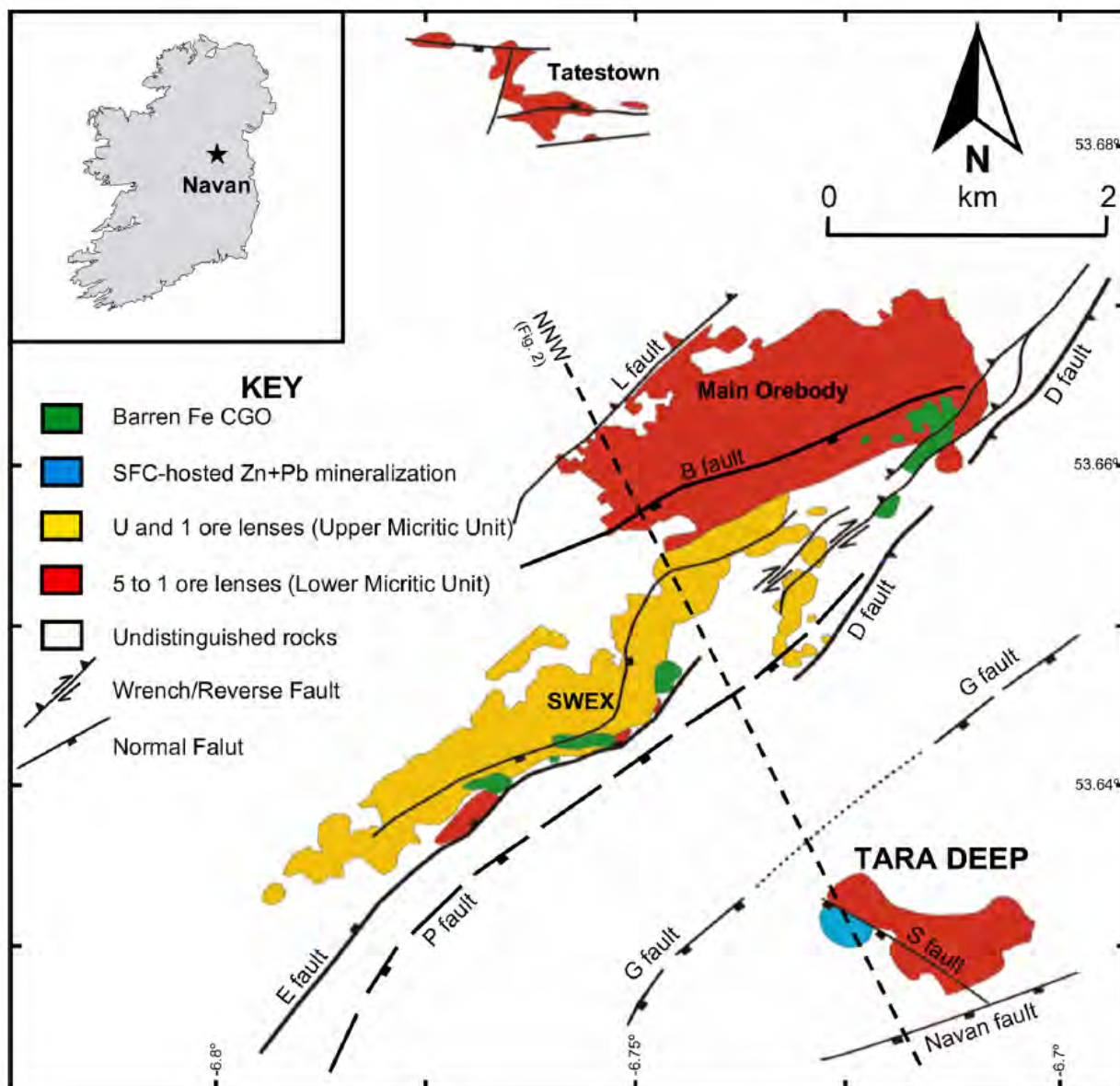
Figure 1: *Map projection of the Tara Deep orebody within the Navan system, including the different deposits and main structural features (modified from Ashton et al. (2015)). SWEX = Southwest Extension Orebody; CGO = Conglomerate Group Ore; SFC = 'S' Fault Conglomerate. Location of NNW-SSW section in Fig. 2 shown.*

In the Navan deposit, upper Tournaisian–Lower Visean low-angle submarine slides and debris flows removed part of the earlier Lower Carboniferous sequence (Philcox, 1989) leading to an erosion surface termed the Navan Unconformity. This unconformity is overlain by a sedimentary breccia known as the Boulder Conglomerate (Boyce *et al.*, 1983). The Boulder Conglomerate is overlain by the thick well-bedded Visean sequence of the Fingal Group (Fig. 2a). In the Navan area, this sequence is known as the Upper Dark Limestones (UDL) and comprises well-bedded calcarenites, lutites and silts (Rees,1987; Strogen *et al.*, 1990).

Comprehensive studies of Irish-type deposits include those of Anderson *et al.* (1998), Fallick *et al.* (2001), Boyce *et al.* (2003), Wilkinson *et al.* (2005), Wilkinson & Hitzman (2015), Ashton *et al.* (2015), Torremans *et al.* (2018), Yesares *et al.*

(2019). In general terms, these deposits are understood to have formed by replacement of Lower Carboniferous limestones at two distinct stratigraphic levels. Deposits in the northeastern Irish Midlands, are hosted mainly by clean carbonates in the Tournaisian limestone sequence (e.g., Navan; Ashton *et al.*, 2015). Further to the south and west, deposits including Lisheen, Galmoy and Silvermines are hosted by dolomitized Waulsortian limestones (Hitzman *et al.*, 2002; Wilkinson *et al.*, 2005; Yesares *et al.*, 2019). As a general rule, deposits are concentrated near normal faults, which are often associated with the development of Devonian – Carboniferous basins (Wilkinson & Hitzman, 2015). These networks of normal faults are widely accepted as pathways for ascending, warm, metal-bearing but relatively H$_2$S-deficient hydrothermal fluids (Fallick *et al.*, 2001; Gagnevin *et al.*, 2012; Ashton *et al.*, 2015), which had scavenged metal from the underlying Lower Palaeozoic
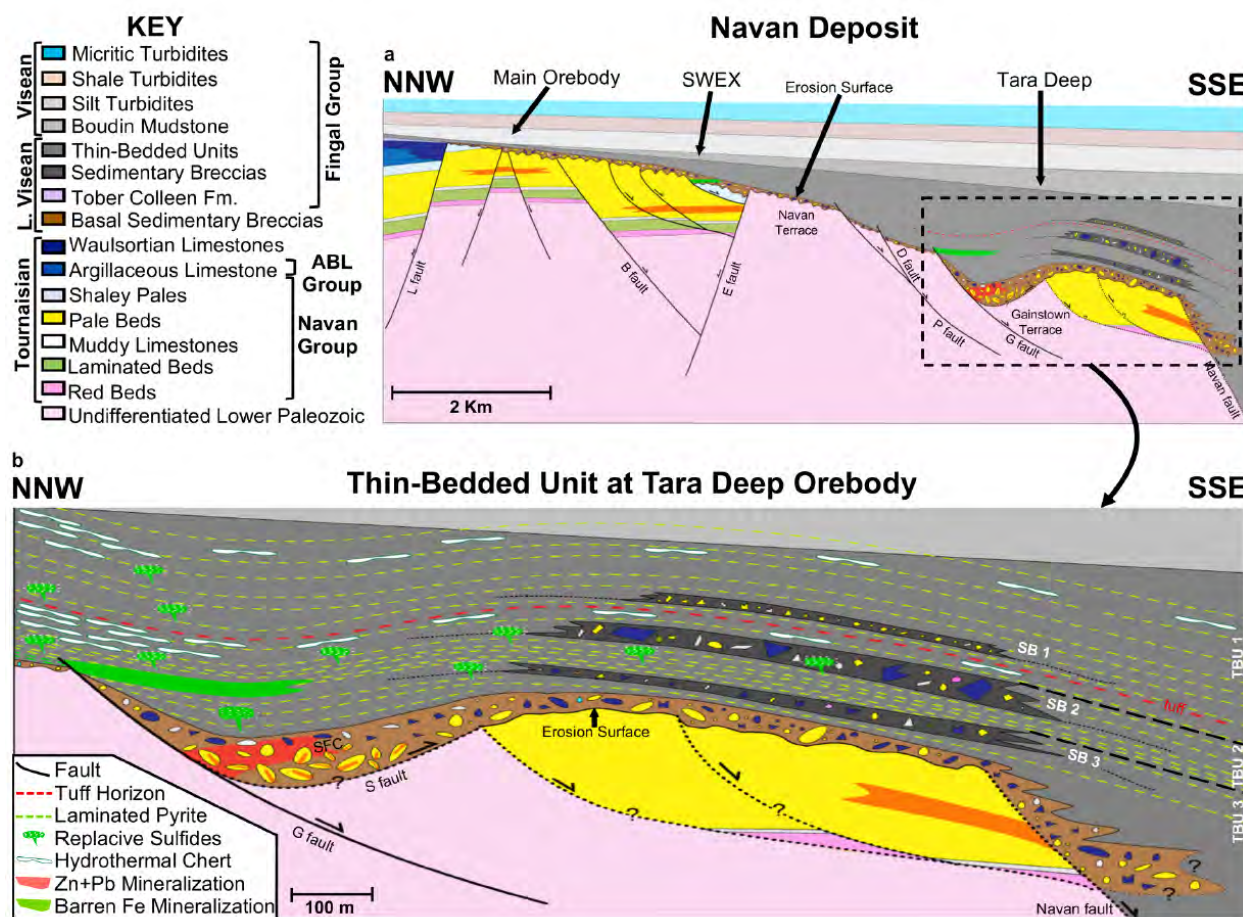
Figure 2. (a) *Cartoon NNW-SSE cross-section across of the Navan deposit, showing the Main Orebody, SWEX and Tara Deep orebody, the overlying Lower Visean mineralized sedimentary units and the main extensional faults active in the Tournaisian to Lower Visean (see Fig. 1 for location);* **(b)** *schematic cross-section detailing the Thin-Bedded Unit and Basal Sedimentary Breccias, their associated mineralization styles and their spatial relationships to the faulted underlying Pale Beds-hosted Tara Deep Zn-Pb mineralization. ABL = Argillaceous Bioclastic Limestone; SWEX = Southwest Extension SFC = 'S' Fault Conglomerate; SB = Sedimentary Breccia; NTBU = New-Thin Bedded Unit.*

basement (Mills *et al*., 1987; Everett *et al*., 2003; Wilkinson *et al*., 2005; Walshaw *et al*., 2006; Yesares *et al*., 2019). These mixed with cooler, hypersaline brines associated with dissolved sulphate, which was reduced to sulphide by BSR processes at or near the site of sulphide precipitation (Anderson *et al*., 1998; Blakeman *et al*., 2002; Ashton *et al*., 2015).

The Navan deposit is relatively well studied based mostly on structural, stratigraphic, petrologic and geochemical analyses of both the Main Orebody and South West Extension (SWEX) (Fig. 1) (Ashton *et al*., 1986; Anderson *et a*l., 1998; Gagnevin *et al*., 2012; Ashton *et al*., 2015). In general, the deposits at Navan are associated with ENE-trending extensional faults associated with the development of the NW margin of the Dublin basin (Wilkinson & Hitzman, 2015; Ashton *et al*., 2015; Yesares *et al*., 2019), (Figs. 1 and 2a). The deposits are hosted mainly by clean carbonates in the Tournaisian Pale Beds limestone sequence (Fig. 2a) (Anderson *et al*., 1998) and consist of stratabound bodies or lenses, composed mainly of sphalerite and galena (Anderson *et al*., 1998). At Navan, the occurrence of sulphide clasts in the overlying Boulder Conglomerate indicates a Lower Visean minimum age for the mineralization (Fig.

2a) (Ford, 1996; Ashton *et al.,* 2003; Ashton *et al.*, 2015).

Samples and methods

The geological observations presented here have been carried out during exploration drilling at the Tara Deep deposit conducted by Boliden Tara Mines. About 270 samples were obtained from 19 previously logged drill cores which encompass all the differentiable lithofacies, mineralization styles and host rocks. About 200 samples of mineralized core drilled from the Lower Visean *syn*-rift UDL sequence overlying the Tara Deep deposit were prepared as polished thin sections for petrographic study by transmitted and reflected light microscopy at University College Dublin (UCD), Ireland. Of these, 120 samples were used for detailed mineralogical and textural studies using a SEM-EDS JEOL JMS-5410 equipped with a Link Oxford microanalyzer in UCD.

Eight polished sections containing sulphides were selected for electron microprobe analysis (EPMA) at the University of Huelva, Spain. The chemical compositions were determined using a JEOL JXA-8200 Super Probe Electron Probe Micro-
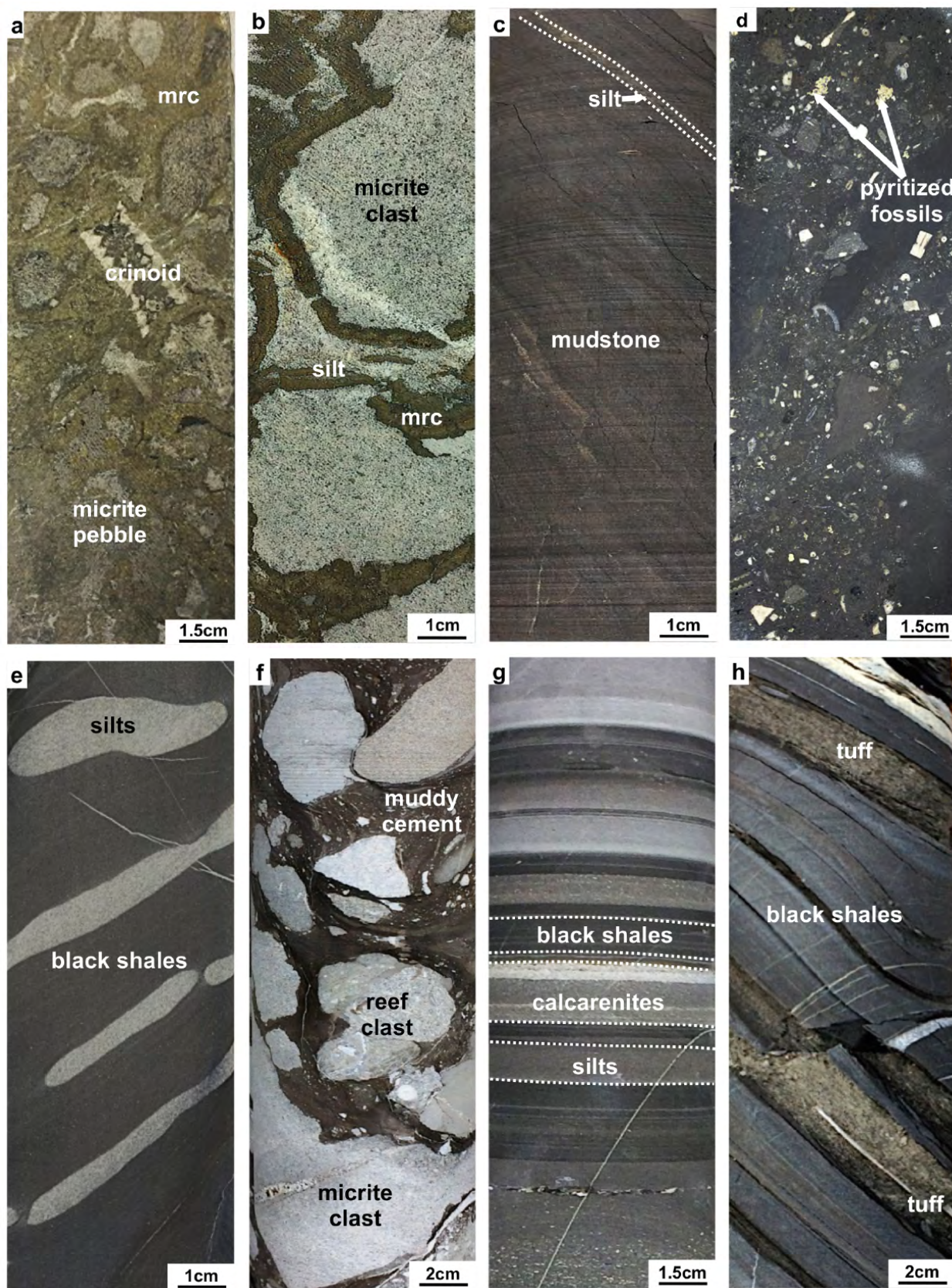
Figure 3. *Main N-TBU and BSB facies of the Tara Deep area. (**a**) BSB including reef and micrite pebbles and fossils cemented by marcasite (mrc); (**b**) SB-3 composed of Waulsortian reef pebbles cemented by marcasite; (**c**) N-TBU-3 comprising black mudstone and thin silt layers; (**d**) SB-2 including micrite pebbles and pyritized fossils; (**e**) N-TBU-2 including black shales and silts, both showing nodular or boudin morphology; (**f**) SB-1 composed of both micrite and Waulsortian reef pebbles included in a muddy cement; (**g**) N-TBU-1 comprising alternating sequences of calcarenites, calsilts and black shales; (**h**) Tuffaceous horizon in black N-TBU-1 black shales.*

Analyzer. The measurements were performed on carbon-coated polished sections using an accelerating voltage of 20 kV, with 20nA beam current, 30 sec counting time for the peaks and 10 sec for the background measurements. The spots analyses were selected using backscattered electron (BSE) images. Concentrations of Ag, Sb, Cd, Bi, Te, As, Mo, Sn, Co, Se, Ni, Au, Cu, Zn, Fe, Pb, Hg and S in sulphides were determined by wavelength-dispersive spectroscopy (WDS). Up to 83 EPMA analyses of sulphides have been obtained. Routine data reduction, including full matrix (ZAF) corrections, were performed. The X-ray lines employed were $K\alpha$ for S, Co, Fe, Ni, Cu and Zn; $M\alpha$ for Hg, Au, Pb and Bi; $L\alpha$ for Te, Sn, Mo, As, Ag, Se and Sb; and $L\beta$ for Cd. The standard materials and corresponding detection limits for each analysed element were as follows: Ag (Ag), 120 ppm; Sb (Sb_2S_3), 270 ppm; Cd (CdTe), 120 ppm; Bi (Bi_2S_2), 120 ppm; Te (CdTe), 120 ppm; As (Zn_3As_2), 220 ppm; Mo (Mo), 100 ppm; Sn (SnSe) 100 ppm; Co (Co), 100 ppm; Se (SnSe), 300 ppm; Ni (Ni), 100 ppm; Au (Au), 120 ppm; Cu (Cu), 140 ppm; Zn (ZnS), 140 ppm; Fe (FeS_2), 110 ppm; Pb (PbS), 400 ppm; Hg (HgTe), 120 ppm; and S (FeS_2), 50 ppm. Sample concentrations below these detection limits are not presented. Minimum, maximum and mean concentrations were calculated using only analyses having values above the detection limited.

In situ laser ablation S isotope analyses were made on polished blocks of 19 sulphide-rich N-TBU samples, selected on the basis of the petrological study. The analyses were made using the techniques of Kelley & Fallick (1990), Kelley *et al.* (1992) and Wagner *et al.* (2002). Data reduction and details of the calculation of the small (typically < 1‰) laser-induced fractionation is discussed in detail in Kelley & Fallick (1990), Fallick *et al.* (1992) and Wagner *et al.* (2002). The polished blocks were inserted into a laser chamber which was evacuated and subsequently filled with an excess of oxygen gas. A Spectron Laser 902QCW Nd:YAG laser (1 W power) then facilitated combustion of the sulphide within a ~50 μm diameter spot, which was then tracked across each sulphide until enough gas had been accumulated for mass spectrometric analysis (Fallick *et al.*, 1992). The released SO_2 gas was purified in a standard S vacuum extraction line, on-line to the mass spectrometer. Determination of the S isotope composition of the purified SO_2 gas ($\delta^{66}SO_2$) was carried out using a VG SIRA II gas mass spectrometer, monitored and calibrated using standards NBS-123 (17.1‰), IAEA-S-3 (–32‰) and the internal lab standard, CP-1 (-4.6‰). Sixty-seven S isotope compositions were calculated relative to Canon Diablo Troilite (CDT) and are reported in standard $\delta^{34}S$ notation. Reproducibility based on complete duplicate analyses (including combustion) was better than ±0.3‰.

An oxygen isotope study on 9 quartz grains from banded sulphide-bearing cherts from the N-TBU was also completed at SUERC. O isotope ratios were measured on 1 mg aliquots of sample by the laser fluorination method of Sharp (1990) as modified for chlorine trifluoride by Macaulay *et al.* (2000). A carbon dioxide laser acting as a controlled and localizable heat source was used to bring the quartz to incandescence whereupon it reacted with the atmosphere of fluorinating reagent and released oxygen. The oxygen was purified cryogenically and by passing through an in-line Hg diffusion pump from where

it was transferred to the vicinity of a heated rod of platinized graphite. The resultant carbon dioxide was transferred to a capacitance manometer where the chemical yield was measured as a monitor of complete reaction. Data are reported in the conventional $\delta^{18}O$ notation relative to Vienna Standard Mean Ocean Water (V-SMOW). Analysis of an international silicate reference standard NBS 28 quartz gives $\delta^{18}O$=+9.6‰V-SMOW and the precision for isotopically homogeneous material is ±0.2‰ or better at one sigma. Crystallization temperatures were modelled from quartz-water fractionation curves using the equation of Matsuhisa *et al.* (1979).

Geology of the Tara Deep deposit

Tara Deep is located ~2 km south of the Navan deposit, at a depth of 1.1–1.9 km (Figs. 1 and 2a).

Stratigraphy

In the Tara Deep area, the Carboniferous stratigraphic succession comprises the Tournaisian basal limestone sequence, which forms part of the Navan Group, overlain by the Visean marine succession comprising the Fingal Group (Fig. 2a).

The lower parts of the pre-rift Tournaisian stratigraphy resemble those reported in the Navan deposit (Ashton *et al.*, 2018), including the marginal marine to shallow water deposits of the Navan Group, such as Red Beds, Laminated Beds, Muddy Limestone, micrites and dolomitized calcarenites and oolites (Fig. 2). Unlike at Navan, these are overlain by a succession of massive grainstones (Philcox, unpublished). The beginning of major rifting in the area, associated with the formation of the Dublin Basin (Ashton *et al.*, 2015), led to uplift of the Navan Group footwall and consequent gravitational instability resulted in low-angle slides and sedimentary breccias. Denudation of the Navan and Cruicetown groups led to ~500m of pre-rift stratigraphy being removed (Fig. 2).

Further collapse events at Tara Deep are recorded by the deposition of polymict breccias, higher in the stratigraphy, interpreted as a succession of submarine debris flows and fault-talus breccias (Fig. 2). The polymict Basal Sedimentary Breccia ('BSB'), is stratigraphically the lowest breccia and is composed of heterometric clasts from a few centimetres to several meters (Fig. 2b), including Waulsortian limestone clasts >15 m in drill-core and with occasional Pale Beds fragments (Fig. 2). To the NW of the Tara Deep deposit, there is a distinctly different sedimentary breccia termed the 'S Fault' Conglomerate ('SFC'). Here, the most common clasts are Pale Beds with only minor Waulsortian limestone (Fig. 2b). The relationship between the BSB and SFC remains unclear.

The SFC and BSB (Fig. 3a) are overlain by the N-TBU of the UDL, which includes the higher lenses of polymict submarine debris flows interbedded with distal calc-turbidites and shales (Fig. 2b and 3b-h). The N-TBU at Tara Deep ranges between 120 and 600m in thickness and can be divided into four distinct facies separated by sedimentary breccias. N-TBU-4 is currently the lowest recognised member and is broadly equivalent to the more regional Tober Colleen Formation. Its maximum thickness is currently unknown, and it is dominated by

occasionally burrowed, dark grey to black, massive, argillaceous micrites. A poorly preserved, polymict sedimentary breccia (SB-4), separates N-TBU-4 from the overlying N-TBU-3 and comprises Waulsortian and Pale Beds fragments cemented by black lutites (Fig. 2b) The overlying N-TBU-3 consists of a sequence of laminated black shales and silts (Fig. 3c). Another polymict sedimentary breccia (SB-3) (Fig. 3b), separates N-TBU-3 from N-TBU-2 which again comprises laminated shales and silts but now showing both nodular and boudinage textures (Fig. 2b and e). SB-2 overlies N-TBU-2 and hosts coarse Waulsortian and Pale Beds clasts encompassed by dark lutites, as well as large rafts of N-TBU-4 and N-TBU-3 (Fig. 2b and d). The uppermost N-TBU-1 consists of centimetric fining-upward sequences of bedding parallel alternating layers of calcarenites, calcsiltites and black shales (Fig. 3g and h). The lower part of the N-TBU-1 includes a cm-scale tuffaceous horizon, and the stratigraphically highest sedimentary breccia (SB-1) (Fig. 2b, f and h). SB-1 is composed mostly of irregular Pale Beds fragments cemented by argillite and silts (Fig. 2b and f). N-TBU-1 exhibits a gradational contact with the overlying Boudin Shale member of the UDL and is commonly marked by both reddish Mn staining (best observed in somewhat weathered core) and several lenses of banded sulphide-rich cherts, from 0.5 to 3 cm in thickness (Fig. 2b).

The part of the UDL overlying the N-TBU at Tara Deep is formed mainly of distal calc-turbidites and minor black shales resembling those in the wider Navan area (Fig. 2) (Philcox, 1984). Due to continuing extensional activity into the Middle Visean in the area (Ashton *et al*., 2015; Ashton *et al*., 2018), the whole UDL at Tara Deep is considered part of the *syn*-rift sedimentary record.

Structural features

The Tara Deep deposit lies between two major extensional structures, which formed part of the northern margin of the Dublin Basin during the Lower Visean. The ENE-trending 'G' Fault forms the northern boundary, while the southern limit is defined by a larger structure, the sub-parallel Navan Fault, which has a displacement of at least 3 km (Ashton *et al.*, 2018). The structural Gainstown Terrace formed by the Navan and 'G' faults is dissected by the high-angle 'S' Fault, a NNW-striking, westerly dipping structure (Figs. 1 and 2) (Coller unpublished work; Ashton *et al*., 2018). A further terrace (the Navan Terrace) lies to the north between the 'G' Fault and the similarly oriented 'P' Fault. North of the 'P' Fault is a distinct horst formed between the 'P' and 'E' Faults, the latter structure being a NW dipping major normal fault, locally forming the southern margin of the Southwest Extension of the Navan deposit (Figs. 1 and 2a).

Based on seismic and drilling data, the 'S Fault' does not appear to significantly displace the Lower Visean Basal Sedimentary Breccia and associated erosion surface (Fig. 2b), and the N-TBU clearly drapes over the 'S' Fault as in a monocline. This suggests that the 'S' Fault was active before the deposition of lower UDL. Regionally, seismic data shows that the ABL thickens across extensional faults, strongly suggesting that was the point at which extension started to accelerate. It is therefore likely that the 'S'' Fault also initiated at that time. The 'G' Fault is seen to displace significant thicknesses of N-

TBU and records continued extension into the Visean. Due to inversion the exact history of the Navan Fault is unclear. Several low-angle faults can be interpreted from the drill-hole data that affect the Pale Beds. Locally observed shearing within the basal Navan Group may suggest structural contacts with the underlying Lower Palaeozoic basement (Fig. 2) (Ashton *et al.*, 2018), although these are currently not fully defined.

Mineralization styles

Mineralization at Tara Deep is unevenly distributed throughout the stratigraphy from the Lower Micrite to the N-TBU (Fig. 3). Based on the host rock, mineralogical and textural features, three different styles of mineralization can be distinguished:

Zn-Pb mineralization hosted by the Pale Beds (Navan Group)

This comprises approximately 92% of the total resource at Tara Deep (Ashton *et al.*, 2018). This part of the deposit shows a stratabound geometry, approximately 50m in thickness. It is hosted by both the Lower and Upper Micrites and, where mineralization is strongest, by the intervening dolomite as well. Disposition is controlled by low-angled SE-dipping faults (Figs. 1 and 2).

Key features are comparable with those previously reported for the Main Orebody and the SWEX (see Ashton *et al*., 2015 and references therein). The Lower Micrite hosts the highest grades comprising replacive sphalerite, galena, pyrite and marcasite. The Upper Micrite shows variable but lower grades dominated by sulphide veining. The mineralization hosted by the Pale Beds at Tara Deep is equivalent to the 5 Lens in the Main Navan Orebody, which hosts 70% of the pre-mining ore (Ashton *et al.*, 2015).

Zn-Pb mineralization hosted by the S Fault Conglomerate

Mineralization hosted by the SFC in the NW sector (Figs. 1 and 2) comprises approximately 8% of the total resource at Tara Deep. This SFC includes a significant amount of re-worked mineralized clasts cemented by later sulphides (Figs. 3a and 4). Of crucial importance is that some of these detrital clasts occur in the conglomerate just above the mineralized horizons, thereby strongly suggesting that previously mineralized Pale Beds contributed to the load. This also suggests that the mineralizing episode spanned the formation of the 'S' Fault Conglomerate, and that therefore a Lower Visean minimum age for the onset of mineralization at Tara Deep can be defined. This is comparable with the minimum age for the onset of mineralizing activity at the Navan deposit from similar evidence. Therefore, the mineralizing systems at both deposits remained active throughout the rifting event. Due to its location in the common hanging-wall of the 'G' and 'S' faults, the origin of this sedimentary breccia is interpreted as a proximal fault talus (Figs. 2 and 3a). This mineralization is similar to that hosted by the Boulder Conglomerate in the Navan Deposit in the hanging-wall of the T Fault (Ashton *et al.,* 2015).

### Mineralization hosted by the N-TBU

About 200m thick sub-economic mineralization has been identified in the overlying N-TBU (Figs. 2, 3b-3h and 5a-5l). It
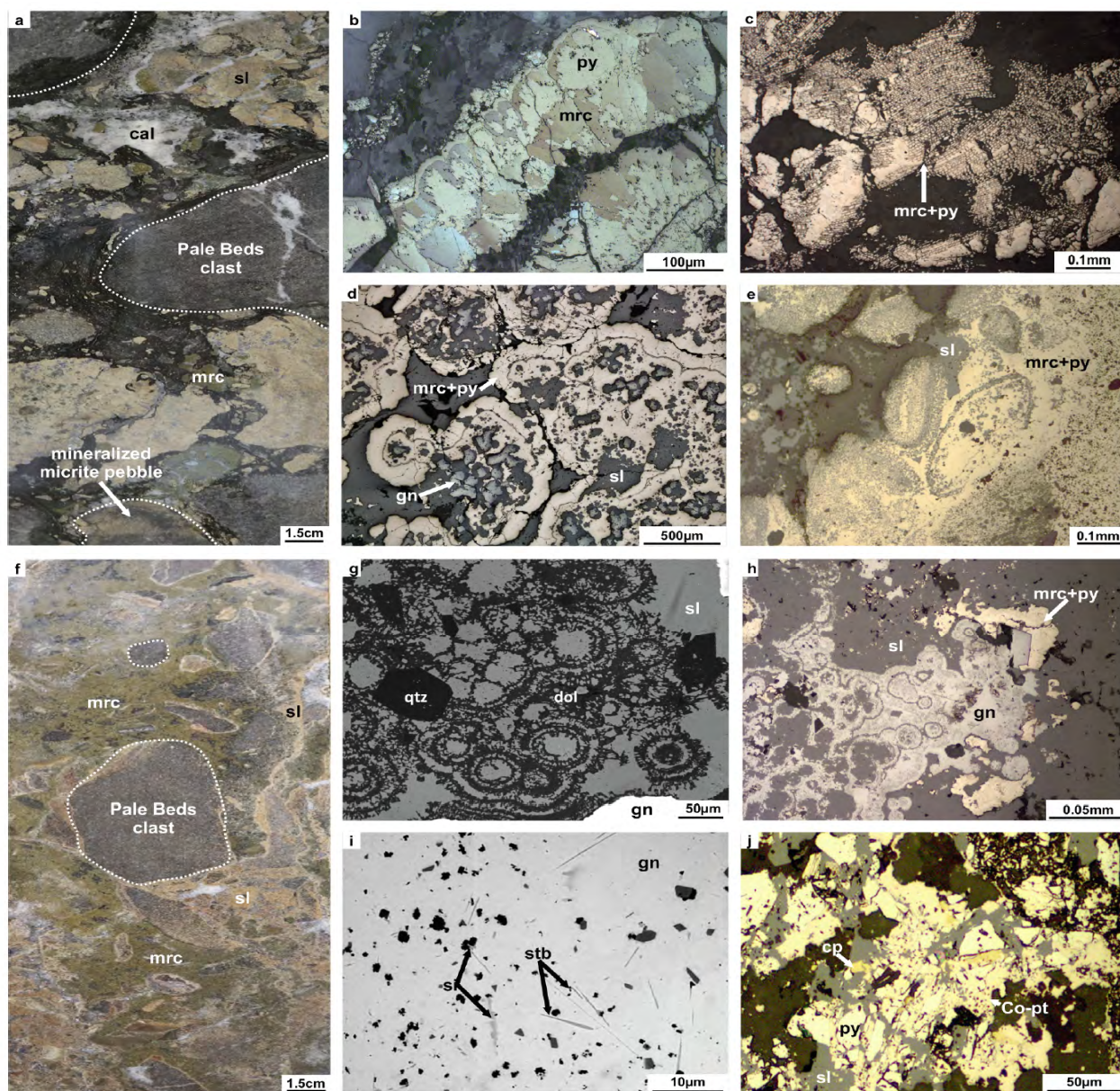
Figure 4. *Drill core reflected light and backscattered electron (BSE) images of the Zn + Pb mineralization hosted in the SFC at Tara Deep. (a) Both mineralized and unmineralized Pale Beds clasts cemented by sphalerite (sl), marcasite (mrc) and calcite (cal) (modified from Yesares et al. (2019)); (b) pyrite (py) partially corroded, replaced and overgrown by later marcasite; (c) marcasite (mrc) and pyrite replacing wood cells; (d) colloform marcasite and pyrite included in later skeletal galena (gn) and sphalerite; (e) pyritized microforaminifera replaced by later sphalerite; (f) SFC including unmineralized Pale Beds clasts with sphalerite and marcasite filling open spaces (modified from Yesares et al. (2019)); (g) dolomite (dol) replaced by colloform sphalerite; (h) marcasite and pyrite botryoids partially replaced by colloform galena, in turn replaced by interstitial sphalerite; (i) fine grained siegenite (si) and stibnite (stb) inclusions in galena; (j) interstitial chalcopyrite (cp), sphalerite and Co-pentlandite filling open spaces in pyrite.*

comprises 0.5–15 cm thick bedding-parallel layers of framboidal pyrite, minor disseminated sphalerite and other rare sulphides extensively distributed throughout the N-TBU (Fig. 5a-g). Here, associated bioclastic layers show a high degree of pyritization (Fig. 5h-k). In addition, minor replacive sulphides and sulphide-rich cherts have been observed, including chalcopyrite, galena and stibnite (Figs. 6 and 7). Similar to the Navan deposit, thin bands of sphalerite and galena occur near the base of the N-TBU, very close to the SFC, and laminated pyrite is also common in mudstone layers in the overlying Upper Dark Limestone. However, the vertical extent of this type of mineralization at Tara Deep is very much larger (100s of meters). The better development of this mineralization style at Tara Deep may indicate a longer life for the mineralizing processes at this locality than elsewhere in the mineralizing system.
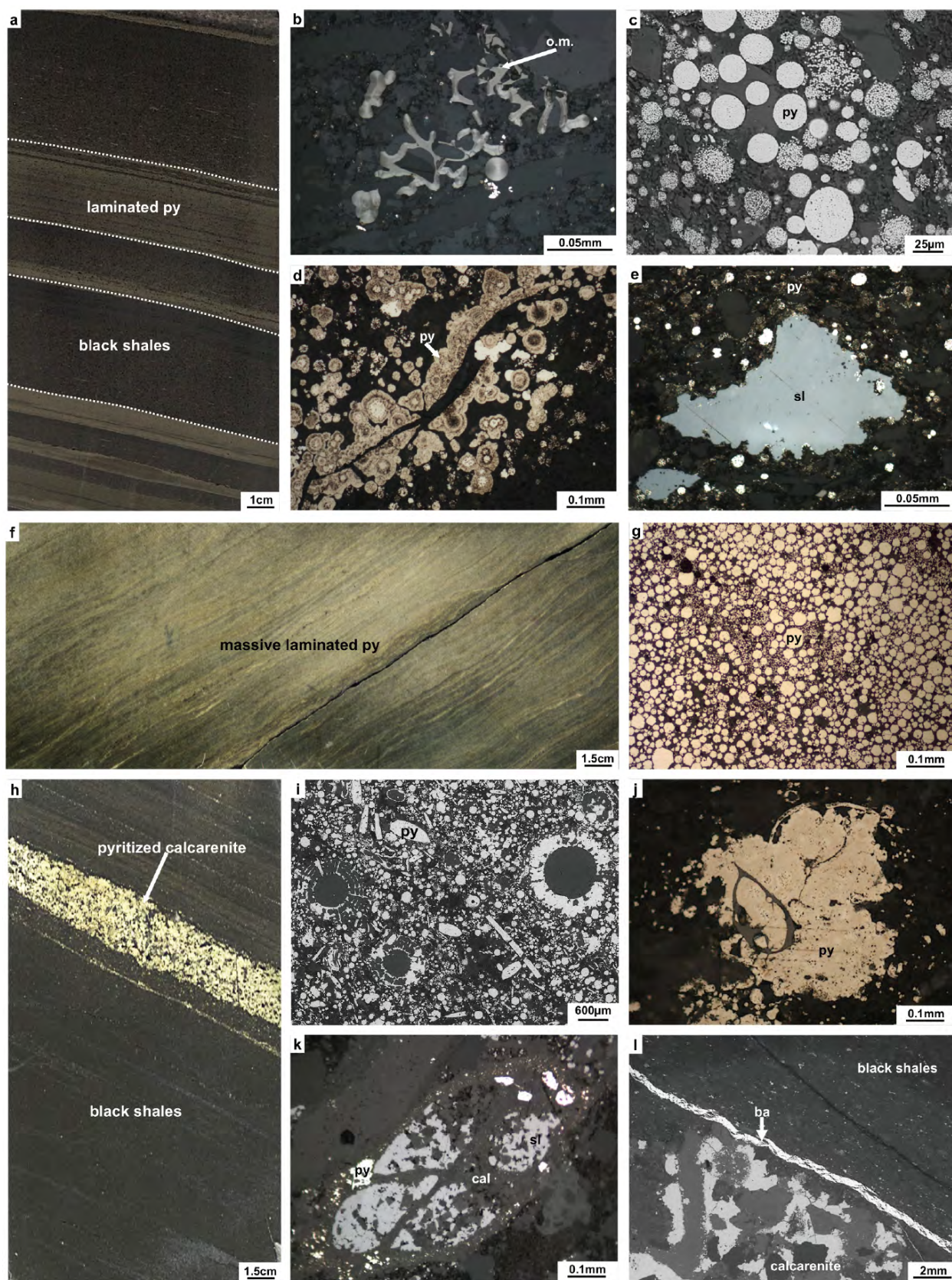
Figure 5. *Drill core reflected light and BSE images of both laminated pyrite and pyritized fossil assemblages in the Tara Deep N-TBU. (a) Black shales replaced by ~0.5 to 1.5 cm layers of fine-grained pyrite (py) parallel to bedding; (b) relict organic matter (o.m.) included in black shales; (c) laminated framboidal pyrite hosted in black shales; (d) colloform pyrite replacing framboids along a fracture; (e) sphalerite (sl) replacing framboidal pyrite; (f, g) partially recrystallized massive laminated pyrite; (h) pyritized calcarenite layer included in black shales; (i) pyritized fossils (mainly radiolaria) in a calcarenite layer; (j, k) microforaminifera and radiolaria replaced by pyrite and sphalerite; (l) late barite (ba) vein cutting both laminated pyrite and pyritized fossils assemblages.*
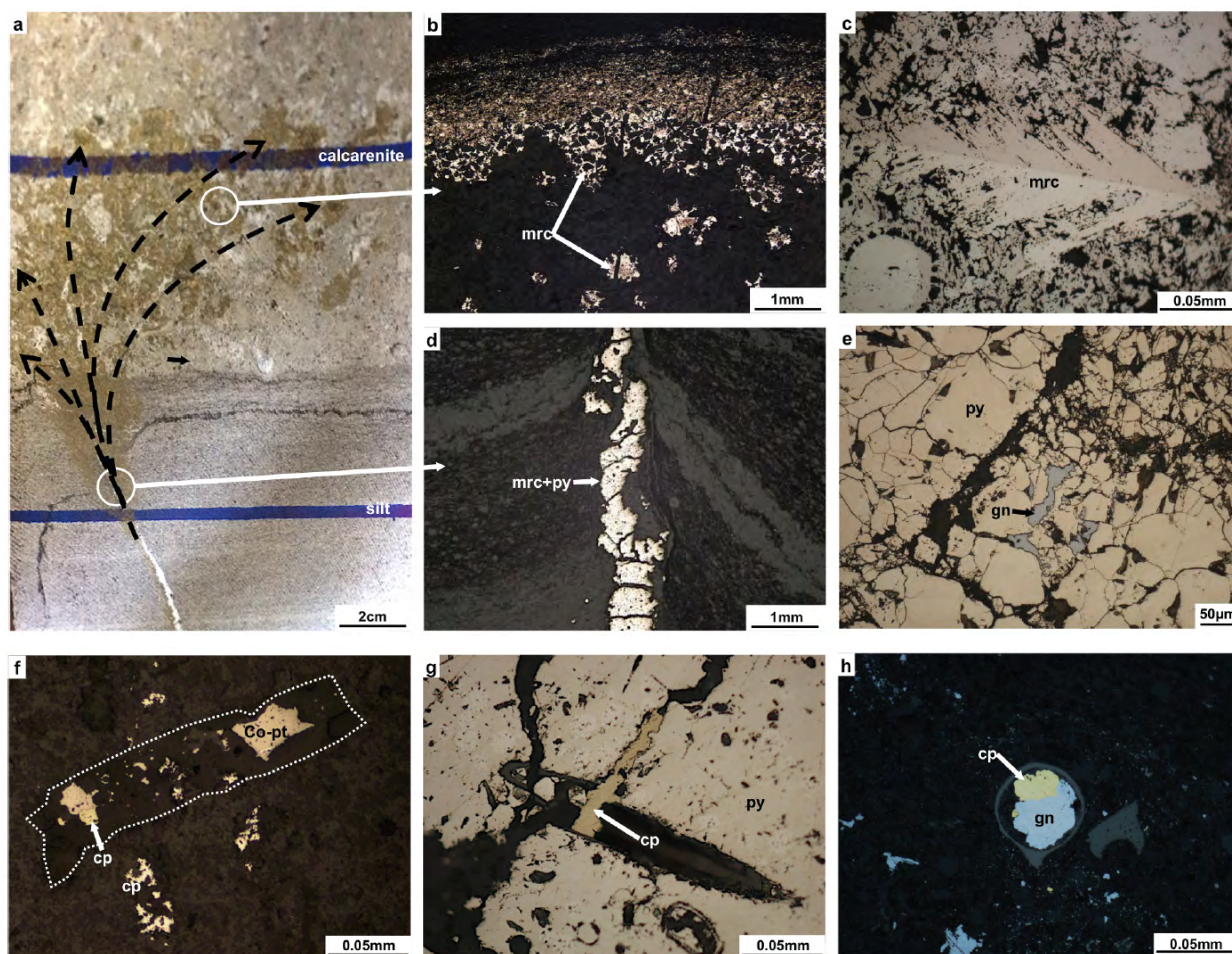
Figure 6. *Drill core reflected light and BSE images of the replacive assemblage in the Tara Deep N-TBU. (**a**) Marcasite (mrc) and minor pyrite (py) filling fractures and interstices in both silts and calcarenite; (**b**) marcasite enclosing a bioclast layer parallel to bedding; (**c**) skeletal marcasite replacing radiolaria in calcarenite; (**d**) marcasite and pyrite vein crosscutting the bedding and deforming the sediments and associated earlier laminated pyrite; (**e**) interstitial galena (gn) in pyrite; (f) fine-grained Co-pentlandite (Co-pt) and chalcopyrite (cp) replacing fossils; (**g**) interstitial chalcopyrite in pyrite; (**h**) chalcopyrite and galena replacing a microforaminifera internal mold,*

Mineral assemblages

The *syn*-rift Lower Visean sedimentary rocks at Tara Deep host two main mineralization styles: (1) economic mineralization in the SFC (Figs. 2, 3a and 4); (2) sub-economic mineralization hosted by the N-TBU, overlying the BSB and SFC (Figs. 2, 3b-f, 5, 6 and 7). Each of them comprises a variety of mineral associations detailed in sub-sections 5.1 and 5.2, respectively. Table 1 (pyrite), Table 2 (sphalerite) and Table 3 (other minerals) summarize the ranges of mineral major and minor element compositions determined by EPMA. Full analytical data are provided in Appendixes 1, 2 and 3.

Mineralized SFC

Clasts forming the breccia, including Pale Beds, Waulsortian Limestone and mineralized material, show dissolution-replacement textures, where irregular corroded clast edges have been replaced mainly by a newly formed generation of sulphides (Figs. 3a, 4a-f). This sulphide assemblage consists of marcasite, pyrite, sphalerite and galena (Fig. 4b-e and g-h),

with minor chalcopyrite, siegenite, Co-pentlandite and stibnite (Fig. 4i and j).

Later sulphides show a wide range of textures. Marcasite replaces pyrite and both minerals replace bioclasts and occur in colloforms and alternating microbands (Fig. 4a-e). Galena appears mainly as skeletal aggregates, colloforms, filling interstices in marcasite and pyrite aggregates, and as euhedral crystals including fine-grained exsolutions of stibnite and siegenite (Fig. 4d, h and i). Chalcopyrite occurs in small amounts intergrown with Co-pentlandite and cementing brecciated pyrite (Fig. 4j). Paragenetically late sphalerite appears infilling and replacing earlier marcasite, pyrite, galena, chalcopyrite and Co-pentlandite (Fig. 4d, h and j). In addition, colloform sphalerite has been observed associated with dolomite (Fig. 4g).

Pyrite shows slight enrichment in As, and a high Co/Ni ratio, with a mean value of 2. Sphalerite is characterized by low Fe (mean 1.7 wt%) and high Cd (mean 0.3 wt%) displaying a mean Zn/Cd ratio of 362. Siegenite contains low Ni (mean of 26.7 wt%) and high Co, Fe and Zn (mean values of 24.9, 6.1
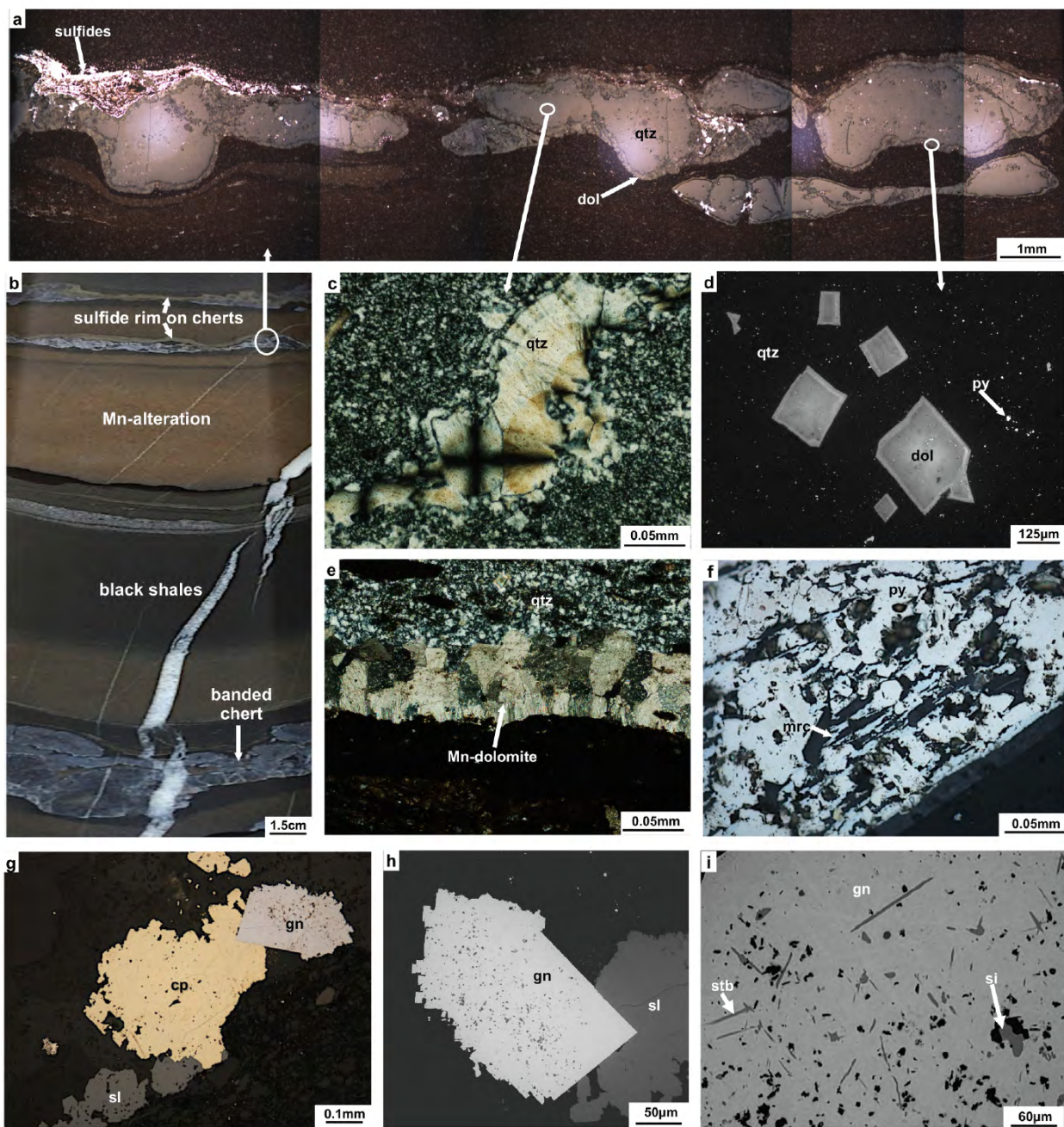
Figure 7. *Drill core reflected light and BSE images of banded sulfidic cherts in the Tara Deep N-TBU. (a, b) Centimetric scale banded cherts included in reddish Mn-rich black shales; (c) chert core comprising microcrystalline quartz (qtz) to radial fibrous crystals forming chalcedonic colloforms; (d) fine-grained inclusions of euhedral dolomite with Mn-enriched grain boundaries; (e) Mn-rich dolomite (dol) rimming chert; (f) fine-grained bird's eye marcasite (mrc) and pyrite (py) rimming chert; (g, h) subhedral aggregates of sphalerite (sl), chalcopyrite (cp) and galena (gn) along chert boundaries; (i) detail of a galena crystal showing very fine exsolved siegenite (si) and stibnite (stb).*

and 0.95 wt%, respectively). Stibnite is notably enriched in metals and metalloids such as Sn, Fe, Pb, Bi, Se and As, with mean values of >0.1 wt%.

Mineralized N-TBU

Petrographic analyses have revealed a texturally complex mineralogy, composed mainly of pyrite with subordinate marcasite, sphalerite, galena, chalcopyrite, stibnite, Co-pentlandite and siegenite (Figs. 5, 6 and 7). Calcite, ankerite, quartz and

barite are the main gangue minerals associated with the sulphide phases. Based on their mineralogical and textural features, four sulphide assemblages have been identified:

Laminated pyrite

This is the major assemblage extending over a 200m thickness of the N-TBU (Fig. 2b). Laminated pyrite is mostly composed of 0.5–15 cm thick bedding-parallel layers of pervasively disseminated pyrite and subordinate sphalerite, closely associated

Wt.%	S	Fe	Zn	Pb	Cu	Co	Ni	Sb	As	Te	Au	Ag	Hg	Se	Bi	Cd	Mo	Sn	Total	Co/Ni
Pyrite matrix in SFC (n = 3)																				
Min	51.226	46.796	0.045	n.d.	0.092	0.024	0.017	n.d.	0.014	n.d.	0.024	0.034	0.043	n.d.	0.038	0.046	n.d.	n.d.	99.122	0.727
Max	53.007	47.813	0.194	n.d.	0.092	0.057	0.033	n.d.	0.023	n.d.	0.024	0.034	0.043	n.d.	0.038	0.220	n.d.	n.d.	100.188	3.353
Mean	52.027	47.251	0.120	n.d.	0.092	0.041	0.025	n.d.	0.019	n.d.	0.024	0.034	0.043	n.d.	0.038	0.149	n.d.	n.d.	99.595	2.040
Std. Dsv.	0.816	0.467	0.075	n.d.	n.d.	0.017	0.008	n.d.	0.005	n.d.	n.d.	n.d.	n.d.	n.d.	n.d.	0.084	n.d.	n.d.	0.491	1.313
Framboidal laminated Pyrite (n = 38)																				
Min	49.938	44.967	0.014	n.d.	0.006	0.010	0.012	0.028	0.013	0.016	0.014	0.012	0.012	0.030	0.015	0.005	0.024	0.015	98.071	0.375
Max	53.503	49.375	0.108	n.d.	0.108	0.112	0.207	0.042	0.388	0.084	0.089	0.192	0.061	0.046	0.066	0.666	0.257	0.085	100.976	4.579
Mean	52.290	46.730	0.046	n.d.	0.054	0.054	0.058	0.035	0.110	0.039	0.038	0.074	0.029	0.036	0.039	0.139	0.088	0.053	99.475	1.395
Std. Dsv.	0.865	1.034	0.031	n.d.	0.030	0.028	0.051	0.006	0.113	0.023	0.022	0.057	0.015	0.006	0.015	0.143	0.098	0.032	0.810	1.228
Pyritized fossils (n = 6)																				
Min	52.355	46.129	0.026	n.d.	0.015	0.013	0.010	0.030	0.017	0.012	n.d.	0.020	n.d.	n.d.	0.011	0.024	0.011	0.015	99.014	0.542
Max	53.548	47.793	0.075	n.d.	0.073	0.081	0.050	0.030	0.030	0.024	n.d.	0.024	n.d.	n.d.	0.110	0.104	0.011	0.015	101.586	3.800
Mean	53.015	47.061	0.047	n.d.	0.041	0.044	0.027	0.030	0.024	0.018	n.d.	0.022	n.d.	n.d.	0.050	0.055	0.011	0.015	100.331	2.061
Std. Dsv.	0.492	0.670	0.023	n.d.	0.025	0.028	0.017	n.d.	0.007	0.006	n.d.	0.002	n.d.	n.d.	0.041	0.032	n.d.	n.d.	1.068	1.474
Pyrite included in replacive assemblage (n = 4)																				
Min	51.946	45.476	0.064	n.d.	0.085	0.022	0.015	n.d.	0.022	n.d.	0.033	n.d.	n.d.	n.d.	0.071	0.019	0.064	0.043	98.440	5.733
Max	52.848	46.494	0.132	n.d.	0.091	0.086	0.015	n.d.	0.029	n.d.	0.033	n.d.	n.d.	n.d.	0.071	0.124	0.064	0.099	98.858	5.733
Mean	52.387	45.944	0.099	n.d.	0.088	0.060	0.015	n.d.	0.026	n.d.	0.033	n.d.	n.d.	n.d.	0.071	0.066	0.064	0.071	98.684	5.733
Std. Dsv.	0.404	0.463	0.030	n.d.	0.003	0.031	n.d.	n.d.	0.004	n.d.	n.d.	n.d.	n.d.	n.d.	n.d.	0.048	0.000	0.028	0.199	–
Pyrite rimmed banded sulfide-rich cherts (n = 6)																				
Min	52.497	46.400	0.028	n.d.	0.024	0.079	0.010	0.040	0.016	0.019	n.d.	0.020	n.d.	n.d.	0.016	n.d.	0.090	0.016	99.670	1.960
Max	53.003	47.957	0.054	n.d.	0.090	0.100	0.050	0.040	0.150	0.030	n.d.	0.020	n.d.	n.d.	0.150	0.099	0.090	0.016	100.912	10.000
Mean	52.725	47.368	0.041	n.d.	0.054	0.091	0.022	0.040	0.069	0.025	n.d.	0.020	n.d.	n.d.	0.074	0.043	0.090	0.016	100.448	6.546
Std. Dsv.	0.202	0.620	0.012	n.d.	0.028	0.008	0.017	n.d.	0.056	0.006	n.d.	n.d.	n.d.	n.d.	0.053	0.037	n.d.	n.d.	0.471	3.109

n.d.: not detected

Table 1: *Statistical summary of pyrite EPMA analyses of the different mineral assemblages identified in the Lower Visean at Tara Deep*

Wt.%	S	Fe	Zn	Pb	Cu	Co	Ni	Sb	As	Te	Au	Ag	Hg	Se	Bi	Cd	Mo	Sn	Total	Zn/Cd
Sphalerite matrix in SFC (n = 3)																				
Min	32.721	0.525	64.698	n.d.	0.107	0.008	0.042	n.d.	0.026	0.016	n.d.	n.d.	n.d.	0.065	0.015	0.102	0.020	n.d.	100.355	106.236
Max	33.043	2.741	66.692	n.d.	0.223	0.264	0.294	n.d.	0.028	0.016	n.d.	n.d.	n.d.	0.065	0.015	0.609	0.041	n.d.	101.104	653.843
Mean	32.893	1.714	65.496	n.d.	0.165	0.122	0.168	n.d.	0.027	0.016	n.d.	n.d.	n.d.	0.065	0.015	0.328	0.031	n.d.	100.739	362.848
Std. Dsv.	0.146	1.004	0.977	n.d.	0.058	0.118	0.126	n.d.	0.001	n.d.	n.d.	n.d.	n.d.	n.d.	n.d.	0.233	0.011	n.d.	0.336	247.299
Sphalerite in laminated pyrite (n = 11)																				
Min	32.619	0.412	63.866	n.d.	0.015	0.005	0.010	n.d.	0.023	0.032	n.d.	0.041	0.021	0.054	0.017	0.143	0.014	0.012	98.751	66.538
Max	33.593	2.601	67.245	n.d.	0.110	0.060	0.011	n.d.	0.064	0.051	n.d.	0.157	0.066	0.053	0.071	0.987	0.069	0.012	101.513	462.727
Mean	33.165	1.178	65.633	n.d.	0.050	0.030	0.011	n.d.	0.045	0.042	n.d.	0.091	0.040	0.056	0.044	0.388	0.039	0.012	100.441	268.363
Std. Dsv.	0.320	0.808	1.291	n.d.	0.036	0.025	n.d.	n.d.	0.018	0.010	n.d.	0.044	0.017	0.002	0.021	0.309	0.023	n.d.	0.850	142.813
Sphalerite associated with pyritised fossils (n = 2)																				
Min	33.046	0.886	64.100	n.d.	0.023	0.044	n.d.	0.033	0.035	0.088	n.d.	n.d.	0.016	0.032	0.046	0.202	0.097	n.d.	99.543	260.224
Max	33.416	1.677	65.056	n.d.	0.031	0.044	n.d.	0.033	0.036	0.088	n.d.	n.d.	0.033	0.032	0.046	0.250	0.097	n.d.	99.604	317.327
Mean	33.231	1.282	64.578	n.d.	0.027	0.044	n.d.	0.033	0.036	0.088	n.d.	n.d.	0.025	0.032	0.046	0.226	0.097	n.d.	99.574	288.775
Std. Dsv.	0.185	0.395	0.478	n.d.	0.004	n.d.	n.d.	n.d.	n.d.	n.d.	n.d.	n.d.	0.009	n.d.	n.d.	0.024	n.d.	n.d.	0.030	28.551
Sphalerite included in replacive assemblage (n = 4)																				
Min	32.705	0.725	63.720	n.d.	0.007	0.030	0.011	0.022	0.042	0.022	n.d.	0.015	0.033	0.042	0.018	0.132	0.059	n.d.	66.759	274.729
Max	33.470	2.599	66.069	n.d.	0.605	0.045	0.041	0.184	0.042	0.041	n.d.	0.221	0.046	0.053	0.095	0.240	0.117	n.d.	67.987	483.439
Mean	33.038	1.545	65.054	n.d.	0.243	0.037	0.027	0.092	0.042	0.032	n.d.	0.092	0.039	0.048	0.056	0.188	0.088	n.d.	67.333	364.577
Std. Dsv.	0.310	0.781	1.129	n.d.	0.249	0.007	0.014	0.076	n.d.	0.010	n.d.	0.092	0.006	0.006	0.031	0.043	0.029	n.d.	0.532	83.406
Sphalerite rimmed banded sulfide-rich cherts (n = 2)																				
Min	32.913	1.644	64.931	n.d.	0.037	0.023	n.d.	0.035	0.054	0.115	n.d.	0.039	0.016	n.d.	0.045	0.163	0.059	0.016	100.369	326.286
Max	32.958	1.712	65.655	n.d.	0.171	0.023	n.d.	0.041	0.054	0.115	n.d.	0.039	0.058	n.d.	0.049	0.199	0.059	0.023	100.587	402.791
Mean	32.936	1.678	65.293	n.d.	0.104	0.023	n.d.	0.038	0.054	0.115	n.d.	0.039	0.037	n.d.	0.047	0.181	0.059	0.020	100.478	364.539
Std. Dsv.	0.023	0.034	0.362	n.d.	0.067	n.d.	n.d.	0.003	n.d.	n.d.	n.d.	n.d.	0.021	n.d.	0.002	0.018	n.d.	0.004	0.109	38.252

n.d.: not detected

Table 2: *Statistical summary of sphalerite EPMA analyses of the different mineral assemblages identified in the Lower Visean at Tara Deep.*

Table 3: *Statistical summary of EPMA analyses on siegenite, stibnite, chalcopyrite and galena from different mineral assemblages identified in the Lower Visean at Tara Deep.*

Wt.%	S	Fe	Zn	Pb	Cu	Co	Ni	Sb	As	Te	Au	Ag	Hg	Se	Bi	Cd	Mo	Sn	Total
Siegenite in SFC matrix (n = 3)																			
Min	41.947	5.821	0.564	n.d.	0.047	24.660	26.493	n.d.	n.d.	n.d.	n.d.	0.150	0.020	0.032	n.d.	0.094	n.d.	n.d.	100.792
Max	42.141	6.431	1.273	n.d.	0.047	25.156	26.923	n.d.	n.d.	n.d.	n.d.	0.150	0.026	0.088	n.d.	0.094	n.d.	n.d.	101.248
Mean	42.027	6.165	0.952	n.d.	0.047	24.911	26.745	n.d.	n.d.	n.d.	n.d.	0.150	0.023	0.060	n.d.	0.094	n.d.	n.d.	101.017
Std. Dsv.	0.093	0.284	0.324	n.d.	n.d.	0.222	0.206	n.d.	n.d.	n.d.	n.d.	n.d.	0.003	0.028	n.d.	n.d.	n.d.	n.d.	0.204
Stibnite in SFC matrix (n = 1)																			
	28.646	0.201	0.011	0.202	0.043	0.028	n.d.	70.940	0.156	n.d.	n.d.	n.d.	n.d.	0.302	0.217	0.065	n.d.	0.413	101.224
Chalcopyrite included in replacive assemblage (n = 5)																			
Min	33.806	31.082	0.049	n.d.	33.587	0.011	0.013	n.d.	0.023	0.030	0.011	0.012	0.023	n.d.	0.012	0.025	0.057	0.018	99.260
Max	34.858	31.659	0.227	n.d.	34.218	0.074	0.033	n.d.	0.045	0.039	0.011	0.050	0.063	n.d.	0.039	0.032	0.057	0.018	100.607
Mean	34.366	31.366	0.140	n.d.	33.956	0.045	0.021	n.d.	0.032	0.035	0.011	0.031	0.046	n.d.	0.026	0.029	0.057	0.018	99.966
Std. Dsv.	0.433	0.218	0.080	n.d.	0.248	0.026	0.010	n.d.	0.011	0.005	n.d.	0.016	0.023	n.d.	0.014	0.004	n.d.	0.018	0.533
Galena rimmed banded sulfide-rich cherts (n = 2)																			
Min	12.928	0.018	0.016	84.410	n.d.	n.d.	0.038	1.682	0.053	0.066	n.d.	n.d.	n.d.	0.379	0.208	0.013	n.d.	0.153	100.759
Max	13.331	0.039	0.103	87.686	n.d.	n.d.	0.038	1.682	0.053	0.066	n.d.	n.d.	n.d.	0.569	0.245	0.108	n.d.	0.153	101.286
Mean	13.130	0.029	0.060	86.048	n.d.	n.d.	0.038	1.682	0.053	0.066	n.d.	n.d.	n.d.	0.474	0.227	0.061	n.d.	0.153	101.023
Std. Dsv.	0.201	0.011	0.044	1.638	n.d.	n.d.	n.d.	n.d.	n.d.	n.d.	n.d.	0.006	n.d.	0.095	0.019	0.048	n.d.	n.d.	0.264
Stibnite rimmed banded sulfide-rich cherts (n = 1)																			
	28.714	0.047	n.d.	0.287	n.d.	n.d.	n.d.	69.603	0.116	n.d.	n.d.	0.006	n.d.	0.432	0.200	n.d.	n.d.	n.d.	99.405

n.d.: not detected

with black shales (Fig. 5a-e). This assemblage, where best developed, can comprise 2–3 m thick massive pyrite bodies, for example in the G fault hangingwall (Figs. 2b, 5f and g).

Pyrite occurs mainly as 5 to 50 μm framboidal aggregates, which are closely associated with relict mature organic matter (Fig. 5b). Framboidal textures have a very high degree of preservation (Fig. 5c), usually with little recrystallization. Occasionally, pyrite has been observed partially recrystallized to colloform texture (Fig. 5d) and euhedral crystals (Fig. 5g). Sphalerite occurs interstitially and replacing pyrite framboids (Fig. 5e). Barite is scarce in the N-TBU but has been recognized as late veinlets crosscutting the laminated pyrite (Fig. 5l).

Pyrite crystals show homogeneous composition. Pyrite is relatively enriched in Co (mean = 0.054 wt%) and exhibits a mean Co/Ni ratio of 1.4. Sphalerite also exhibits homogeneous composition, including low Fe contents (mean = 1.17 wt%) and a low mean Zn/Cd ratio of 268. No compositional zonation has been observed in SEM backscattered studies on pyrite.

Pyritized fossils

Bioclasts forming the calcarenite and calcsiltite layers within the N-TBU show a high degree of pyritization (Fig. 5h). Pyrite and minor sphalerite occur as microfossil replacement, mainly of radiolaria and micro-foraminifera (Fig. 5i-k). This assemblage is widely distributed in the N-TBU, progressively decreasing upwards and closely associated with the laminated pyrite (Fig. 2b).

Pyrite replacing fossils in the N-TBU shows a comparable composition to framboidal laminated pyrite, except for Co and Ni, which show mean Co/Ni ratio of 2. Sphalerite replacing bioclasts is characterized by low Fe and Cd contents (mean values of 1.2 and 0.2 wt%, respectively) and displays a mean Zn/Cd ratio of 288. No compositional zonation has been observed in SEM backscattered studies on pyrite.

Replacive assemblage

This is pervasively distributed throughout the N-TBU, but apparently spatially associated with the area above the intersection of the G and S faults (Fig. 2b). It occurs: (1) parallel to the bedding, in which sulphides are infilling primary porosity, replacing the sediments and overgrowing bioclasts (Fig. 6a-c); and (2) crosscutting the bedding and deforming the sediments and associated earlier laminated pyrite (Fig. 6a, d and e).

The sulphide suite is formed mainly by marcasite showing skeletal textures and/or replacing fossils (Fig. 6c), and by massive pyrite (Fig. 6e and g). Subordinate sulphides consist of micrometric sphalerite, chalcopyrite, galena and Co-pentlandite filling open spaces in marcasite and pyrite or replacing bioclasts (Figs. 6f-h, 7g-h).

Pyrite crystals show a homogeneous composition with a mean Co/Ni ratio of 5. Sphalerite displays a low Fe content (mean = 1.5 wt%) and a high Zn/Cd mean ratio of 364. Chalcopyrite has homogeneous composition and is relatively depleted in
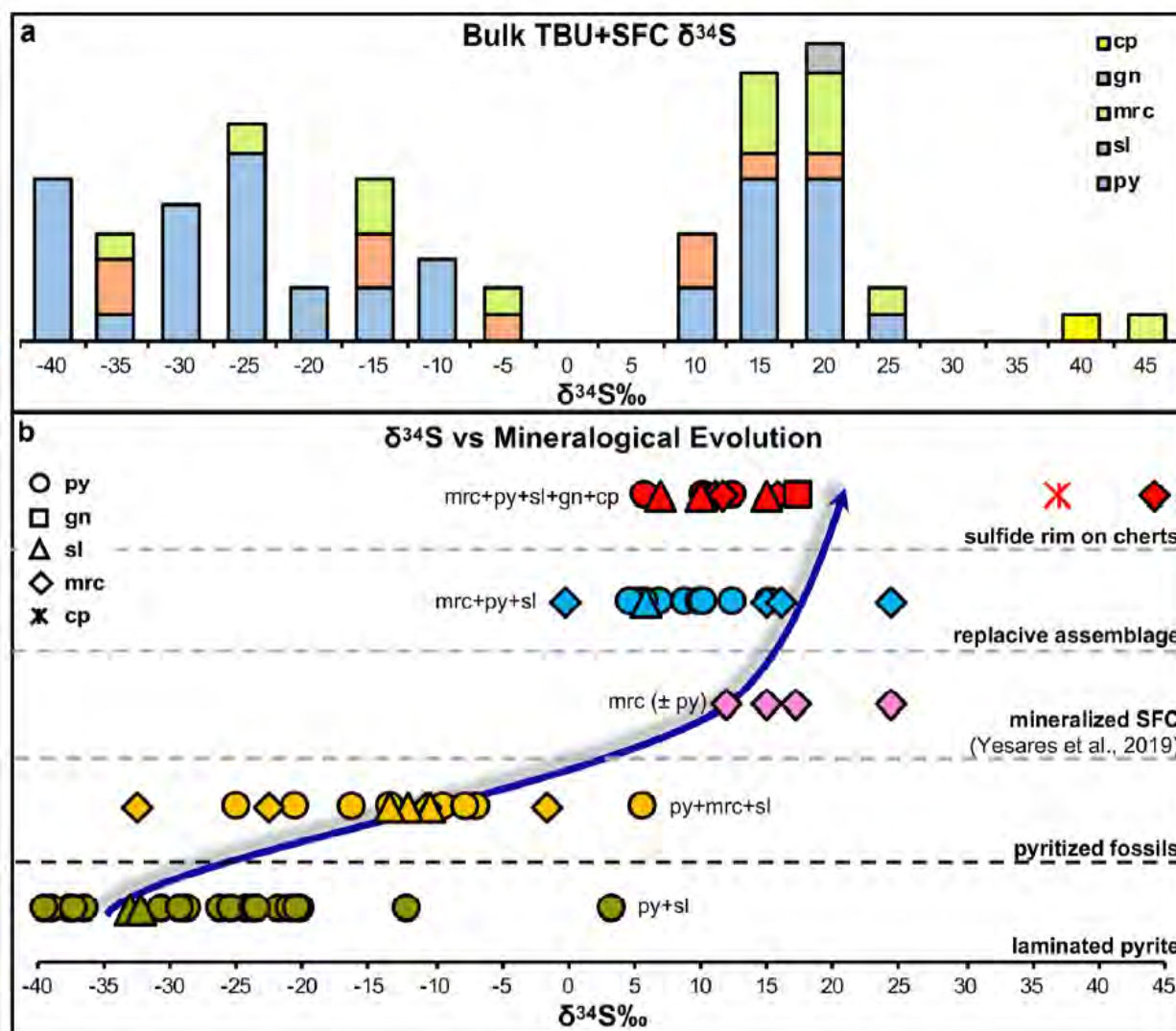
Figure 8. *In-situ δ³⁴S isotope analyses from sulphide assemblages hosted in the Tara Deep N-TBU and SFC. (**a**) Histogram showing the bulk S isotope data distinguished by sulphide phases; (**b**) plot of S isotope data versus mineral assemblages. Abbreviations mrc: marcasite; py: pyrite; sl: sphalerite; gn: galena; cp: chalcopyrite.*

trace elements. No compositional zonation has been observed in SEM backscattered studies on either pyrite or chalcopyrite.

Banded sulphide-rich cherts

These mainly comprise 0.5–3cm thick quartz bands rimmed by coarse carbonates associated with sulphides (Fig. 7a). Banded sulphide-rich cherts are hosted in black shales which show a reddish alteration (Fig. 7b) linked to a high Mn content. They are found systematically at higher stratigraphic levels in N-TBU-1, just below and above the tuffaceous horizon (Fig. 2b). They are most abundant near and above the intersection of the 'G' and 'S' faults.

One of the critical features of the cherts is their relationship with the host sediments. Basal irregularities in the cherts can be seen to have deformed and depressed underlying sediments, whereas overlying sediments are conformably deposited over their tops (Fig. 7a). The silica layers show textures such as microcrystalline and radial fibrous crystals comprising

chalcedonic colloforms (Fig. 7c). Quartz includes fine inclusions of euhedral calcite and minor dolomite, both showing Mn enrichment in their crystal rims (Fig. 7d). Cherts are rimmed by Mn-rich calcite and dolomite linked to a sulphide assemblage including fine bird's-eye marcasite, 5–15 μm euhedral aggregates of pyrite, sphalerite, chalcopyrite and galena which contains very fine siegenite and stibnite inclusions (Fig. 7e-i). In addition, very fine inclusions of euhedral sulphides occur, mainly pyrite included within the cherts (Fig. 7a and d).

Pyrite is relatively depleted in trace elements, although the As content is high (up to 0.15 wt%), with mean Co/Ni ratios of 6.5. Sphalerite is also relatively depleted in trace elements, including low Fe and Cd (means of 1.6 and 0.18 wt%, respectively), and Zn/Cd ratios of 364. Significant trace elements in galena include Bi and Sb, with mean values of 0.22 and 1.68 wt%, respectively. Stibnite grains analysed in the chert rims show comparable Bi concentrations to galena (mean = 0.2wt%). No compositional zonation has been observed in SEM backscattered studies on sulphides.

Table 4: *Sulphur isotope analyses on sulphides from different mineral assemblages identified in the Lower Visean record at Tara Deep.*

Sample ID	Sulphide Assemblage	Mineral	Texture	δ^{34}S (‰)	Sample ID	Sulphide Assemblage	Mineral	Texture	δ^{34}S (‰)
N2409-17c	Matrix in SFC	Marcasite	Replacing pyrite and cementing clasts in SFC	24.6	N2388-6	Laminated pyrite	Pyrite	Recrystalized framboids	-20.8
N2409-17b	Matrix in SFC	Marcasite (+pyrite)	Radial aggregates cementing clasts in SFC	15.2	N2388-8b	Laminated pyrite	Pyrite	Recrystalized framboids	-20.1
N2439-5a	Matrix in SFC	Marcasite	Radial aggregates cementing clasts in SFC	12.1	N2409-1a	Laminated pyrite	Sphalerite (+pyrite)	Interstitial sphalerite replacing framboidal pyrite	-32.8
N2439-5b	Matrix in SFC	Marcasite	Radial aggregates cementing clasts in SFC	17.1	N2409-1b	Laminated pyrite	Sphalerite (+pyrite)	Interstitial sphalerite replacing framboidal pyrite	-32.1
N2409-1a	Laminated pyrite	Pyrite	Framboids	-36.2	N2360-4a	Pyritized fossils	Pyrite	Pyrite infilling fossil internal mold	-6.7
N2409-1b	Laminated pyrite	Pyrite	Framboids	-37.3	N2360-4b	Pyritized fossils	Pyrite	Infilling fossil internal mold	-9.2
N2409- 1c	Laminated pyrite	Pyrite	Framboids	-37.4	N2391-1c	Pyritized fossils	Pyrite	Infilling fossil internal mold	-7.5
N2409-8a	Laminated pyrite	Pyrite	Recrystalized framboids	-11.8	N2391-6a	Pyritized fossils	Pyrite	Infilling fossil internal mold	-15.9
N2394-4a	Laminated pyrite	Pyrite	Framboids	-30.5	N2360-5d	Pyritized fossils	Pyrite	Infilling fossil internal mold	-25.0
N2391-11b	Laminated pyrite	Pyrite	Framboids	-24.0	N2391-6b	Pyritized fossils	Pyrite	Infilling fossil internal mold	-13.4
N2388- 6c	Laminated pyrite	Pyrite	Framboids	-25.9	N2391-11a	Pyritized fossils	Pyrite	Infilling fossil internal mold	-20.5
N2448-01a	Laminated pyrite	Pyrite	Framboids	-19.9	N2360-4c	Pyritized fossils	Marcasite (+pyrite)	Infilling fossil internal mold	-1.3
N0242713	Laminated pyrite	Pyrite	Framboids	-38.8	N2360-5b	Pyritized fossils	Marcasite	Infilling fossil internal mold	-22.4
N02427-13	Laminated pyrite	Pyrite	Framboids	-39.2	N2360-5c	Pyritized fossils	Marcasite	Infilling fossil internal mold	-32.2
N2388-8a	Laminated pyrite	Pyrite	Colloform	-21.5	N2391-1d	Pyritized fossils	Marcasite (+pyrite)	Infilling fossil internal mold	-10.5
N2388-8c	Laminated pyrite	Pyrite	Colloform	-25.2	N2391-1a	Pyritized fossils	Marcasite (+sphalerite)	Infilling fossil internal mold	-13.3
N02439-01	Laminated pyrite	Pyrite	Framboids	-28.5	N2360-5a	Pyritized fossils	Sphalerite	Infilling fossil internal mold	-10.3
N02439-02	Laminated pyrite	Pyrite	Framboids	-23.5	N2391-1b	Pyritized fossils	Sphalerite	Infilling fossil internal mold	-11.9
N2394-4b	Laminated pyrite	Pyrite	Framboids	-37.0	N2391-16a	Replacive assemblage	Pyrite	Euhedral vein crosscutting the bedding	5.9
N2394-4c	Laminated pyrite	Pyrite	Framboids	-29.1	N2391-16b	Replacive assemblage	Pyrite	Euhedral pyrite vein crosscutting the bedding	10.3
N2394-4d	Laminated pyrite	Pyrite	Recrystalized framboids	-23.2	N2409-10a	Replacive assemblage	Pyrite	Euhedral pyrite vein crosscutting the bedding	5.3
N2409-8c	Laminated pyrite	Pyrite	Recrystalized framboids	3.3	N2409-10b	Replacive assemblage	Pyrite	Euhedral pyrite vein	4.9

Sample ID	Sulphide Assemblage	Mineral	Texture	$\delta^{34}S$ (‰)
N2409-5a	Replacive assemblage	Pyrite	Pyrite vein parallel to the bedding; Replacing sediments	8.9
N2409-10c	Replacive assemblage	Pyrite	Pyrite vein parallel to the bedding	7.0
N2360-4c	Pyritized fossils	Marcasite (+pyrite)	Infilling fossil internal mold	-1.3
N2360-5b	Pyritized fossils Marcasite	Marcasite	Infilling fossil internal mold	–22.4
N2360-5c	Pyritized fossils Marcasite	Marcasite	Infilling fossil internal mold	–32.2
N2391-1d	Pyritized fossils	Marcasite (+pyrite)	Infilling fossil internal mold	10.5
N2391-1a	Pyritized fossils	Marcasite (+sphalerite)	Infilling fossil internal mold	13.3
N2360-5a	Pyritized fossils	Sphalerite	Infilling fossil internal mold	-10.3
N2391-1b	Pyritized fossils	Sphalerite	Infilling fossil internal mold	-11.9
N2391-16a	Replacive assemblage Pyrite	Pyrite	Euhedral vein crosscutting the bedding	5.9
N2391-16b	Replacive assemblage Pyrite	Pyrite	Euhedral vein crosscutting the bedding	10.3
N2409-10a	Replacive assemblage Pyrite	Pyrite	Euhedral vein crosscutting the bedding	5.3
N2409-10b	Replacive assemblage Pyrite	Pyrite	Euhedral vein crosscutting the bedding	4.9
N2409-10c	Replacive assemblage	Pyrite	Pyrite vein parallel to the bedding	7.0
N2409-5a	Replacive assemblage	Pyrite	Pyrite vein parallel to the bedding; Replacing sediments	8.9
N2409-5b	Replacive assemblage	Pyrite	Pyrite vein parallel to the bedding; Replacing sediments	10.1
N2409-4c	Replacive assemblage	Pyrite	Pyrite vein parallel to the bedding; Replacing sediments	15.3
N2409- 4d	Replacive assemblage	Pyrite	Pyrite vein parallel to the bedding; Replacing sediment	12.5
N2394-3a	Banded sulphide-rich cherts	Galena	Rimmed chert	17.5
N2409-4e	Replacive assemblage	Pyrite	Pyrite vein parallel to the bedding; Replacing sediments	10.4
N2409-15c	Replacive assemblage	Marcasite (+pyrite)	Marcasite vein parallel to the bedding; Replacing sediments	24.5
N2409-4a	Replacive assemblage	Marcasite	Replacing sediments	16.2
N2409-15a	Replacive assemblage	Sphalerite (+pyrite)	Sphalerite vein parallel to the bedding; Replacing sediments	0.0
N2394-3b	Banded sulphide-rich cherts	Chalcopyrite	Rimmed chert	36.8
N2388-3a	Banded sulphide-rich cherts	Marcasite (+pyrite)	Bird eyes and skeletal	44.2
N2388-3f	Banded sulphide-rich cherts	Marcasite (+pyrite)	Skeletal marcasite rimmed chert	15.7
N2394-1b	Banded sulphide-rich cherts	Marcasite (+pyrite)	Skeletal marcasite rimmed chert	10.3
N2394-1c	Banded sulphide-rich cherts	Marcasite (+pyrite)	Skeletal marcasite rimmed chert	11.2
N2394-1d	Banded sulphide-rich cherts	Marcasite (+pyrite)	Skeletal marcasite rimmed chert	11.6
N2388-3b	Banded sulphide-rich cherts	Pyrite	Euhedral pyrite Skeletal marcasite rimmed chert	5.8
N2409-4b	Banded sulphide-rich cherts	Pyrite	Euhedral pyrite Skeletal marcasite rimmed chert	12.6
N2388-3c	Banded sulphide-rich cherts	Pyrite	Fine euhedral pyrite rimmed chert	10.3
N2388-3d	Banded sulphide-rich cherts	Sphalerite (+Chalcopyrite)	Sphalerite intergrown with chalcopyrite rimmed chert 10.1	10.1
N2394-1a	Banded sulphide-rich cherts	Sphalerite (+Chalcopyrite)	Sphalerite intergrown with chalcopyrite rimmed chert	15.2
N2394-1e	Banded sulphide-rich cherts	Sphalerite	Sphalerite rimmed chert	7.0
N2388-3e	Banded sulphide-rich cherts	Sphalerite	Sphalerite rimmed chert	5.8
N2409-15b	Replacive assemblage	Marcasite (+pyrite)	Marcasite vein parallel to the bedding;	15.2

Sulphide S isotope compositions

The sulphides hosted in the SFC and the N-TBU at Tara Deep have $\delta^{34}S$ values that range from -39.2 to + 44.2‰ (Fig. 8a and Table 4), but compositions vary strongly between different mineral associations (Fig. 8b).

Published S isotope analyses on marcasite (±pyrite) from the SFC matrix at Tara Deep (Fig. 4a-f) reveal high $\delta^{34}S$ values, ranging from 12.1 to 24.6‰ (average of 17.3‰) (Yesares *et al.*, 2019; Fig. 8b and Table 4). Furthermore, S isotope values reported from sulphides in a reworked mineralized clast (Fig. 4a and f) exhibit the typical bimodal distribution described in the micrite-hosted mineralization at both the Tara Deep and Navan deposits (Anderson *et al.*, 1998; Yesares *et al.*, 2019).

Laminated pyrite (Fig. 5a, c, f and g) shows a wide range of low $\delta^{34}S$ values, from -37.4 to 3.3‰ (mean of -24‰) (Fig. 8b). $\delta^{34}S$ values and pyrite recrystallization degree show correlation in each sample. Early framboidal pyrite exhibits the lowest $\delta^{34}S$ values, whereas recrystallized material displays the heaviest compositions (Fig. 5f and g). The $\delta^{34}S$ values of interstitial sphalerite replacing framboids (Fig. 5e) are also low, with mean value of –32.4‰ (Fig. 8b).

Pyritized fossils in calcarenite layers (Fig. 5h, I and j) also have a broad range of $\delta^{34}S$ values from –32.3 to 5.6‰ (mean of -13.2‰) (Fig. 8b), whereas sphalerite replacing fossils (Fig. 5k) shows homogeneous S isotope compositions, with a mean value of -11.8‰ (Fig. 8b).

Sulphides forming replacive assemblages show high $\delta^{34}S$ values (Fig. 8b). Marcasite (±pyrite) (Fig. 6a-e and g) shows a wide range of higher $\delta^{34}S$ values from 0 to 24.5‰ (mean of 18.6‰), whereas pyrite (±marcasite) varies from 4.9 to 15.3‰ (mean value of 9.2‰). One sphalerite grain in the replacive assemblage exhibits a $\delta^{34}S$ values of 5.8‰ (Fig. 8b).

Marcasite and pyrite associated with banded sulphide-rich cherts (Fig. 7a and f) exhibit variable, but systematically high, $\delta^{34}S$ values from 10.1 to 44.2‰ (mean of 18.6‰) and 5.8 to 12.6‰ (mean of 9.6‰), respectively (Fig. 8b). It is worth noting that, due to the close textural links between both Fe sulphides (Fig. 7f), it was impossible to exclusively analyze pyrite or marcasite completely separately. The $\delta^{34}S$ for sphalerite rimming the banded sulphide-rich cherts (Fig. 7g) ranges from 7.0 to 15.2‰ (mean of 10.5‰), while chalcopyrite and galena (Fig. 7g-i) show quite high $\delta^{34}S$ values of 36.8 and 17.5‰, respectively (Fig. 8b).

O isotope composition of banded sulphide-rich cherts

The oxygen isotope compositions of banded sulphide-rich cherts exhibit $\delta^{18}O$ values ranging from 23.7 to 26.3‰ (mean of 25.3‰) (Table 5). Slight vertical $\delta^{18}O$ variations have been observed on cherts from different stratigraphic positions, the lowest values being obtained on the highest stratigraphically cherts just above the tuffaceous horizon.
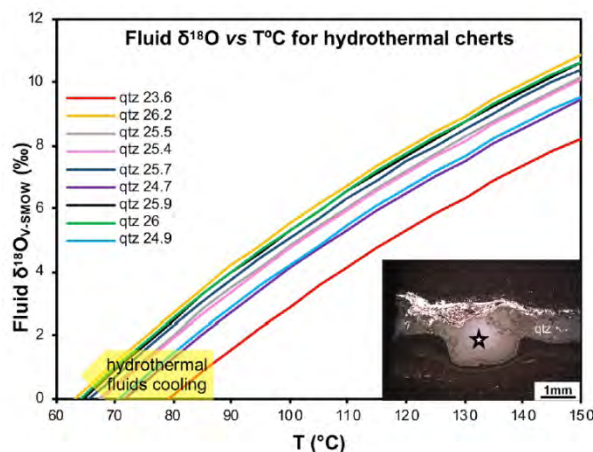
Figure 9: *Fluid vs equilibrium temperature for chert crystallization based on chert $\delta^{18}O$ values and quartz-water fractionation curves using the equation of Matsuhisa et al. (1979).*

Sample ID	δO^{18} SMOW(‰)
N2388-3c	26.3
N2388-3d	25.4
N2409-4c	25.8
N2394-3c	24.8
N2409-5b	26
N2394-1c	23.7
N2394-1d	26
N2409-6c	24.9
N2409-6d	25.5

Table 5: *Oxygen isotope analyses on cherts identified in the TBU hanging wall at Tara Deep.*

The results are used to illustrate possible equilibrium fluid temperature conditions for chert crystallization, by construction of chert-water fractionation curves using the equation of Matsuhisa *et al.* (1979), shown in Fig. 9. We assume equilibrium with seawater with a $\delta^{18}O$ value close to 0, following interpretation of C-O clumped isotope analyses that Lower Carboniferous seawater had a very similar isotopic composition to modern seawater (Henkes *et al.*, 2018). Based on this model, chert crystallization temperatures may range from 65 to 80°C.

Discussion

Tectono-sedimentary environment

The mineralizing processes at Tara Deep were intimately associated with the extensional setting (Fig. 2). Like the Navan deposit, the micrite-hosted mineralization at Tara Deep occurs

near normal faults, which are assumed to be coeval with the development of the Dublin basin (Wilkinson & Hitzman, 2015; Ashton *et al.,* 2015). The mineralizing fluid probably circulated through both the G and Navan faults, and via secondary porosity, resulting in the partial dissolution of earlier carbonates and the precipitation of epigenetic sphalerite and galena mineralization (Anderson *et al.,* 1998; Yesares *et al.,* 2019). At least part of the activity on these faults was coeval with Lower Visean sedimentation (Fig. 2b). Evidence of *syn*-sedimentary faulting includes the thickening of the SFC into the G Fault hanging-wall, which presents a similar relationship to that noted between the Boulder Conglomerate and extensional faults in the Navan deposit (Ashton *et al.*, 2015).

Depositional environment

Traditional SEDEX models propose organic-rich mudstones deposited in a bathypelagic, anoxic, restricted basin in which *syn*-sedimentary deposition of sulphides occurs in a stratified euxinic water column, for example the Black Sea (Goodfellow, 1987; Ozsoy & Unluata, 1997). However, recent models allow more energetic depositional conditions (Schieber *et al.*, 2010; Magnall *et al.*, 2020) beyond the restricted, euxinic basin model (Arthur & Sageman, 1994; Smith *et al.*, 2019). At Tara Deep, the N-TBU stratigraphic record and sedimentary features, such as graded beds, cross laminations and black shales interbedded with siltstone laminae (Fig. 3b-h) are consistent with a non-euxinic low energy and deep marine depositional environment (Miall, 2016). However, the high amount of coarse framboidal pyrite replacing organic matter-rich fine laminae in black shales, that in general show an absence of bioturbation (Fig. 5a, b, c, fa and g), implies anoxic to lower sub-oxic conditions at least below the sediment–water interface (Slack *et al.*, 2004; S´aez *et al.*, 2011; Wilkin *et al.*, 1996; Bond & Wignall, 2010). The scarcity of barite in the N-TBU is consistent with oxygen-poor formation conditions, because the presence or absence of barite is controlled by the activity of sulphate in the water column or in connate waters. In anoxic basins, where all the sulphate has been reduced to sulphide, Ba carried by hydrothermal fluids will be dispersed because of a lack of sulphate to precipitate barite (Johnson *et al.*, 2009 and references therein).

This anoxic environment was occasionally interrupted by the deposition of silts and calciturbidites (Fig. 3c, e and g). These can be interpreted as repeated incursions of oxygenated mass flows derived from a marginal shallow-water oxic environment to the deep-water anoxic environment of the basin floor, probably controlled by seismicity related to extensional faulting or by footwall fault scarp instabilities.

Hydrothermal fluid input

Although framboids are common in diagenetic muds (Taylor & Macquaker, 2000), both laminated pyrite and pyritized fossils hosted in the N-TBU at Tara Deep show evidence of hydrothermal influence. The large amount of Fe and minor Zn, where pyrite is partially replaced by sphalerite (Fig. 5a-g), is widespread for hundreds of metres into the stratigraphic hanging-wall sequence and up to ~2 km laterally (Fig. 2), and includes massive pyrite bodies (Fig. 2b, 5f and g). This high

metal endowment required Fe and Zn supplied by hydrothermal fluids (Lydon, 2007).

Further evidence for hydrothermal activity during and just after N-TBU deposition is the identification of rare chalcopyrite and galena with stibnite and siegenite inclusions, and Co-pentlandite. These sulphides occur as late infillings, veinlets and variable replacive textures, all of them associated with the SFC matrix, banded sulphide-rich cherts and replacive assemblage (Figs. 4, 6 and 7). These assemblages are interpreted to have formed by the reaction of uprising hydrothermal fluids with both SFC-hosted clasts and laminated pyrite in the N-TBU, replacing the lower-temperature sedimentary sulphides by higher-temperature assemblages, consistent with depositional models elsewhere (Goodfellow *et al.,* 1993; Turner, 1991; Kelley & Jennings, 2004). Moreover, open space filling sulphides in breccia matrices suggest that mineralizing fluids flowed throughout the still permeable sediments in early diagenetic stages (Fig. 4a and f; 6a, b and d). Similar high temperature assemblages have been reported linked to feeder zones in other SedEx deposits, such as Rammelsberg, Tharsis, Sullivan and Red Dog (Large & Walcher, 1999; S´aez *et al.*, 1999; Lydon *et al.*, 2000; Kelley & Jennings, 2004).

Pyrite Co/Ni ratios together with absolute values of Co may be suitable for discriminating sedimentary and hydrothermal ore deposits (Xu, 1998; Chowdhury & Lentz, 2017; Maghfouri *et al.*, 2018). According to these authors, sedimentary pyrite has low Co/Ni ratios (generally < 1) and < 100 ppm Co, whereas hydrothermal pyrite is characterized by Co/Ni > 1 and > 400 ppm Co. Laminated framboidal pyrite at Tara Deep shows Co/Ni ratios ranging from 0.3 to 4.5 and Co varying from 100 to 1120 ppm (Table 1 and Appendix 1). Although some framboidal pyrite Co/Ni ratios have apparently sedimentary values (<1), most reflect hydrothermal influence (Co/Ni > 1). Pyritized fossils have a narrow range of Co/Ni values transitional between the sedimentary and hydrothermal pyrite fields and close to Co/Ni = 1 (Table 1 and Appendix 1). This suggests that these pyritized fossils may have formed as a result of the dissolution of sedimentary pyrite by the hydrothermal fluid. All pyrites related to banded sulphide-rich cherts, the replacive association in N-TBU and SFC matrix (Figs. 4, 6 and 7) show Co/Ni ratios ranging from 1.9 to 10 and Co varying from 220 to 1000 ppm (Table 1 and Appendix 1), suggesting a relatively warmer hydrothermal input.

The trace element composition of sphalerite also can be used to constrain the temperature of mineralization (Han, 1994; Gottesman & Kampe, 2007). According to Zhu, (1988), Liu *et al.* (2010), Li *et al.*, (2008), sphalerite in stratabound Pb–Zn deposits is rich in Cd, with Zn/ Cd ratios > 300, and poor in Fe. In contrast, volcanic and magmatic hydrothermal Pb–Zn deposits are rich in Fe, but poor in Cd, with Zn/Cd ratios of < 300. In general, all the measured sphalerites in both the SFC and N-TBU are Fe-poor (mean values ranging from 1.1 to 1.7 wt%; Table 2 and Appendix 2) and Cd-rich (mean Zn/Cd ratios varying from 268 to 364), indicative of an overall low temperature of formation. However, sphalerite from SFC, banded sulphide-rich cherts and replacive association in N-TBU suggest a slightly higher precipitation temperature.

Late sulphide suites in the SFC and N-TBU mineralization display high Bi contents in galena and stibnite (mean of 0.2 wt%) (Fig. 4h, I, 6e, h, 7 g, h and I; Table 3 and Appendix 3). Fleischer (1956) reported a positive correlation between Bi content in sulphides and increasing temperature of formation. Therefore, patterns of high Bi content in sulphide matrix cementing SFC, sulphide-rich cherts and replacive association indicate higher temperatures.

Numerous lenses of banded sulphide-rich cherts mark the N-TBU-1 upper contact with the overlying calc-turbidites of the Fingal Group (Figs. 2 and 7). These cherts occur as finely-laminated thin beds showing soft-sediment deformation (Fig. 7a and b) indicating early silicification at or near the water–sediment interface. Silica, usually as chert, is ubiquitous in most stratiform ores and is in part hydrothermally derived (Yamamoto, 1987; Lei *et al.*, 2019). The source of silica for chert remains problematic and its genesis has been attributed to a variety of processes, such as dissolution of biogenic siliceous remains (e.g., radiolarians, diatomite, sponge and spicules) (Boudreau, 1990); inorganic precipitation from solution (e.g., silica-rich thin-bedded cherts from hot spring waters) (Eker *et al.*, 2012); from fluids related to submarine volcanism (Adachi *et al.*, 1986; Hofmann & Bolhar, 2007); by direct precipitation from Si-oversaturated seawater in hydrothermal environments (Sugitani *et al.,* 1998; Maliva *et al.*, 2005; Tice & Lowe, 2006); or a mixture of both biogenic and inorganic sources (Van Van den Boorn *et al.*, 2007; Van den Boorn et al., 2010; Marin-Carbonne *et al.*, 2012).

The N-TBU-hosted, banded, sulfide-rich cherts are characterized by a lack of siliceous fossils (e.g. diatoms, radiolaria, etc.) and other biological relicts at SEM scale, making a biogenic origin unlikely. The modelled equilibrium fluid temperature of 65 to 80 °C for chert crystallization (Fig. 9) suggests that hydrothermal fluids were relatively warm but cooling by equilibration with seawater. Thus, silica could have precipitated directly from hydrothermal fluids to microcrystalline and botryoidal chalcedony fibres (Fig. 7c), retaining pre-existing dolomite rhombs (Fig. 7d). Moreover, the higher-temperature sulphide assemblage, e.g., chalcopyrite, siegenite, stibnite, galena (Fig. 7f-i), contained by the cherts, also supports relatively higher temperatures of precipitation. All these data suggest that the N-TBU-hosted cherts formed under the strong influence of hydrothermal fluids.

Role of faulting

Faulting at Tara Deep exerted an important control on the mineralizing process during the Lower Visean. For example, although mineralized sediments are widespread within the N-TBU, the pyrite content increases towards the G fault (Figs. 2, 5f and g), leading to massive pyrite lenses a few meters thick, suggesting that this structure acted as an important conduit for hydrothermal fluid flow at least during laminated pyrite formation. The higher temperature assemblages (e.g., stibnite, galena, chalcopyrite, siegenite and Co-pentlandite) (Figs. 4i, j, 6f-h and 7g-i) are also spatially associated with normal faults, and sulphide matrix cementing the SFC (Fig. 4i and j) overlies the S and G faults (Fig. 2). The N-TBU-hosted replacive association occurs as veins crosscutting the bedding (Fig. 6a and d) and filling open spaces in permeable calcarenite layers (Fig. 6a

and b), increasing in abundance toward the intersection of G and S faults. Therefore, higher temperature assemblages provide evidence of sub-seafloor replacement by the mineralizing fluid flowing through both normal faults and permeable sediments (e.g., tectonic breccias and calcarenites). Although these assemblages do not display a stockwork geometry, they may be comparable from a mineralogical and geochemical perspective to feeder mineralization elsewhere (Goodfellow, 2004; Large *et al.*, 1996; Large *et al.*, 2005), where elevated concentrations of some metals and metalloids (Cu, Co, Ni, As, and Sb) are typically more abundant close to vent systems (Sangster, 2018; Torremans *et al.*, 2018). The cherts and associated sulphides (Fig. 7) are interpreted as hydrothermal exhalites formed in an extensional regime because they occur close to, and increase in abundance, above the intersection of the 'G' and 'S' faults. Both the hydrothermal cherts and the higher temperature sulphide assemblage show a similar lateral distribution pattern controlled by the 'G' and 'S' faults.

The geometry of these structures and their relationships to the Navan Fault are compatible with the faulted basin-margin architecture proposed for SEDEX systems, with at least 2 to 5km of *syn*-rift sediments, and where hydrothermal discharge to the seafloor was commonly focused at the intersection of extensional and transform faults (Lydon, 1995; Leach *et al.*, 2005).

Evolution of mineralizing fluids

Although no fluid inclusion data yet exist from the Tara Deep deposit, the temperature and salinity of the fluids at the nearby Navan deposit have been constrained by several studies (Braithwaite & Rizzi, 1997; Everett & Wilkinson, 2001; Peace *et al.*, 2003). The wide range of salinities and temperatures are consistent with fluid mixing (Anderson *et al.*, 1998; Wilkinson, 2010). A basement-equilibrated, relatively high-temperature, low-salinity, H_2S-poor, metal-bearing fluid mixed with a cooler, high-salinity, connate brine considered to be associated with BSR (Ashton *et al.*, 2015 and references therein). Given the similarities in mineralogy, $\delta^{34}S$ values, gross geometry and timing, it is unlikely that the fluids generating the Tara Deep deposit were vastly different.

However, the relative scarcity of base metals in the N-TBU (Fig. 5) may be due to the circulation of metal-exhausted, hydrothermal fluids, or to a fall-off in temperature and/or salinity, and thus the Cl- activity, in the later stages of hydrothermal fluid circulation, thus precluding the effective transport of metals (Leach *et al.*, 2005). Based on mineralogy, textures and S isotopes, the large amount of early, low $\delta^{34}S$, framboidal pyrite and pyritized fossils (Figs. 5 and 8) suggests that early hydrothermal fluids were acidic and H_2S poor. In addition, the strongly negative $\delta^{34}S$ values of most framboidal pyrite (mean -24.0‰) and pyritized fossil (mean -13.2‰) samples indicate that most of their contained S was ultimately BSR-derived.

The preservation of higher, almost all positive, $\delta^{34}S$ values (up to 44‰; Fig. 8) is restricted to later sulphides linked to the hydrothermal cherts and replacive associations in both the mineralized SFC and N-TBU (Figs. 4, 6 and 7). In this scenario, a suitable source for such heavy S may be thermochemical sulphur reduction (TSR) of contemporaneous seawater (Magnall *et al.*, 2016; Sangster, 2018). Moreover, extremely high S

isotope ratios measured in both chalcopyrite and marcasite ($\delta 34S$ = 36 and 44 ‰, respectively) suggest periods of intense hydrothermal activity and high TSR rates. Alternatively, isotopically heavy S may have been derived by hydrothermal fluid leaching of pyrite from underlying Lower Palaeozoic rocks (Anderson *et al.*, 1989). These pyrites have extremely variable S isotope compositions, including a substantial proportion with positive $\delta^{34}S$ values and including maximum $\delta^{34}S$ values of ~ +60‰ (Anderson *et al.*, 1989; Boyce *et al.*, 1994). Furthermore, textural links between cherts and high- $\delta^{34}S$ chalcopyrite, galena, stibnite and siegenite (Fig. 7g-i) also suggest relatively hot fluids able to transport Si, Cu, Co, Sb, Bi (Fournier, 1985; Seward *et al.*, 2014; Moroni *et al.*, 2019). The presence of cherts with marcasite rims (Fig. 7a-f) also implies their crystallization from acidic fluids (Murowchick & Barnes, 1986; Hopkinson *et al.*, 1999). This process would also explain the presence of minor late barite veins (Fig. 5l) because Ba is soluble in reduced and acidic solutions (Lydon, 1983; Cooke *et al.*, 2000).

Metal deposition

The precipitation of sulphides from hydrothermal fluids is generally related to processes that influence the stability of metal complexes. The main mechanisms that cause destabilization of metal complexes and ore precipitation include fluid boiling (immiscibility), fluid mixing, decreases in temperature, pressure, and salinity, and fluid-rock interactions (Hemley *et al.*, 1992; Zhai *et al.*, 2011; Seo *et al.*, 2012; Peng *et al.*, 2016).

Under anoxic conditions, BSR is the most likely process to reduce seawater sulphate to H_2S (Goodfellow & Jonasson, 1984; Large *et al.*, 2005), which is then able to be fixed by reactive $Fe2+$ provided by the halide complexes of the hydrothermal fluid and precipitated as framboidal pyrite (Fig. 5a-c) (Goodfellow, 2000; Large *et al.*, 2005). The wide range of low $\delta^{34}S$ values preserved in framboidal pyrite (-38.8 to 3.3‰; Fig. 8) represent a large offset from the $\delta^{34}S$ value of coeval seawater sulphate (i.e., up to 60‰; Kampschulte *et al.*, 2001), suggesting a large isotopic fractionation in pore fluids under open-system conditions (i.e., sulphate resupply > sulphate consumption) (Kaplan & Rittenberg, 1964; Canfield & Thamdrup, 1994). Since H_2S is produced by BSR within the first 2m of the sediment column, even where overlain by oxic water, sulphide precipitation will always occur within the anoxic sediment regardless of the origin of the metal-bearing fluid (Goodfellow & Jonasson, 1984; Large *et al.*, 2002; S´aez *et al.,* 2011). By analogy, an effective metal trap in the N-TBU resulted from interactions between early diagenetic and hydrothermal processes. Metalliferous fluids further ascended into the subsurface anoxic environment, impregnating the organic-rich muds where pyrite and minor sphalerite were precipitated, leading to the formation of laminated pyrite facies (Fig. 5a-g) and pyritized fossils (Fig. 5h-k). Sulphide textures, mineral assemblages and trace element compositions similar to those described in both the laminated pyrite and pyritized fossils have also been described in Rammelsberg, Tharsis, McArthur River and Ab-Bagh deposits (S´aez *et al.*, 2011; Large & McGoldrick, 1998; Movahednia *et al.*, 2020).

Metal precipitation related to the later higher-temperature assemblages in both the SFC and N-TBU may have been triggered by a decrease in fluid temperature by interaction with the cooler sedimentary and diagenetic environment. Both skeletal marcasite, common in the replacive assemblages (Fig. 6c) and chert crystallization temperatures (Fig. 9), suggest rapid cooling of acidic hydrothermal fluids (Chen *et al.*, 2010; Heaney,1993; Hopkinson *et al.*, 1999). Moreover, marcasite showing birds-eye texture as rims on cherts (Fig. 7f) indicates slight oxidation processes (Ramdohr, 1980). In this scenario, the cooling of the fluids reduces the solubility of metals (Brimhall & Crerar, 1987; Reed & Palandri, 2006), consequently resulting in the deposition of higher-temperature sulphide assemblages (Figs. 4i-j, 6f-h and 7g-l). The textural relationships between these higher temperature sulphide assemblages and the hosting sediments suggests that these formed by both replacement of the sediments during early diagenesis (e.g., sulphide veins crosscutting and deforming the bedding and infilling primary sediments porosity; Fig. 6), as well as on or near to the seafloor, recorded by the deposition of hydrothermal cherts coevally with sulphides (Fig. 7). Moreover, the precipitation of minor late barite veins (Fig. 5l) in the N-TBU reflects some minor sulphate activity in connate waters (Johnson *et al.*, 2009). Some Ba carried by hydrothermal fluids might have reacted with the remaining, probably isotopically heavier, sulphate to precipitate barite in the latest stages.

Links between sulphides hosted by Pale Beds, SFC and N-TBU

Overall, SEDEX systems are typically long-lived (Goodfellow & Lydon, 2007). Hydrothermal activity commonly continues after sulphide formation, forming post-ore mineralized sediments and widespread alteration extending for hundreds of metres into the stratigraphic hanging-wall sequence and up to several kilometres laterally from the deposit (Lambert & Scott, 1973; Large *et al.*, 2002; Mukherjee &Large, 2017).

At Tara Deep, mineralization hosted by the N-TBU clearly shows that mineralizing fluids continued circulating after the formation of the sulphides hosted by the Pale Beds. Sedimentation of overlying breccias and N-TBU was cyclic. Sulphide clasts included in the sedimentary breccias (Fig. 4a and f), coupled with alternating discrete laminated pyrite layers (Fig. 5a), suggests repeated erosion of mineralized Pale Beds, diagenetic sulphide formation in black shales, and re-mineralization overprinting both sulphide clast and laminated pyrite at times of fault movement (Fig. 2) with intervening, tectonically quiescent periods. Active faulting may have facilitated Pale Beds mineralization by allowing mixing of metal-bearing and sulphide-bearing fluids. Mineralization in both the SFC matrix and the N-TBU therefore represent post-ore hydrothermal activity of the Tara Deep Pale Beds-hosted deposit, with hydrothermal cherts the most distal part of the system.

Overall, the mineralization in and above the SFC and BSB represents a hanging-wall halo to the Tara Deep Pale Beds-hosted Zn-Pb mineral deposit. Exhausted and/or weaker brine exhalations were likely sourced from the G, and possibly S, faults and were probably relatively dilute compared to the mineralizing brines that deposited the Pale Beds-hosted mineralization. Most geological features included in the hanging-wall halo are similar to those described in Tom, Meggen, Sullivan and
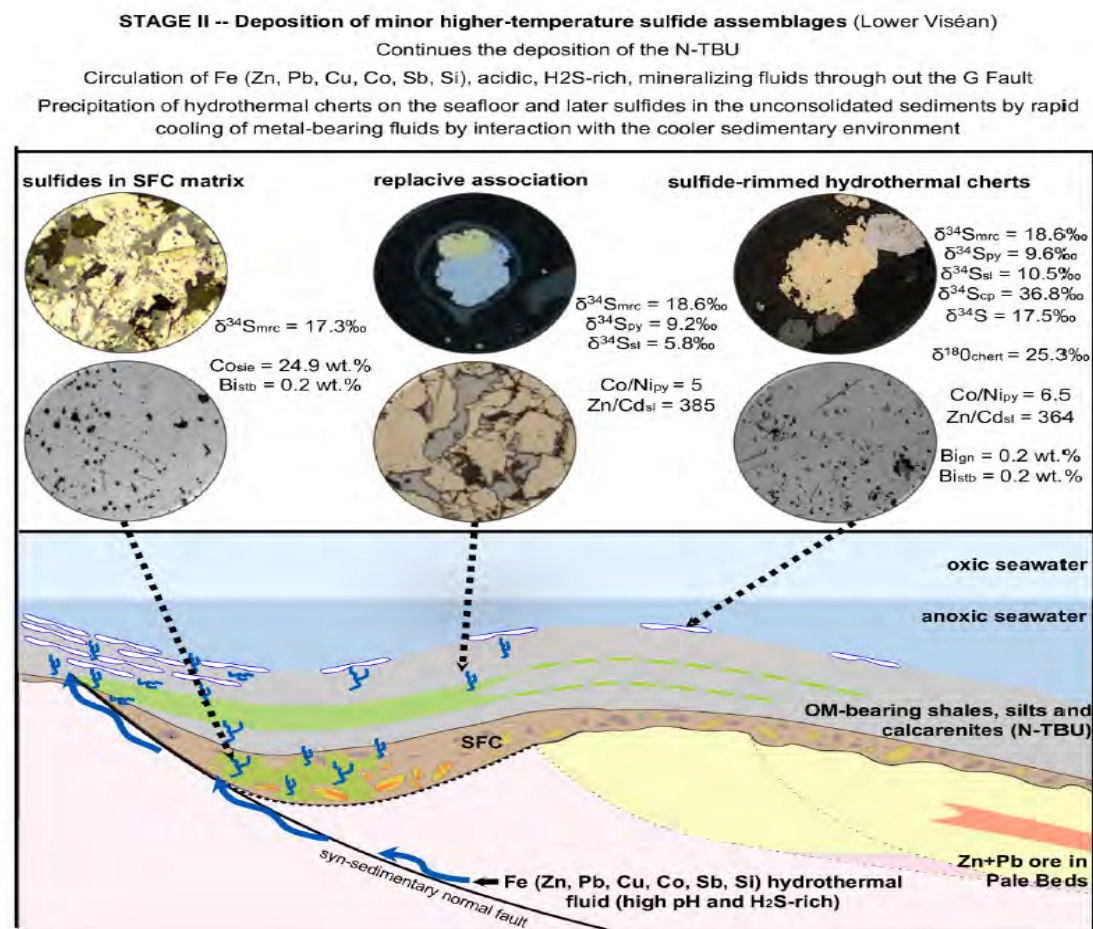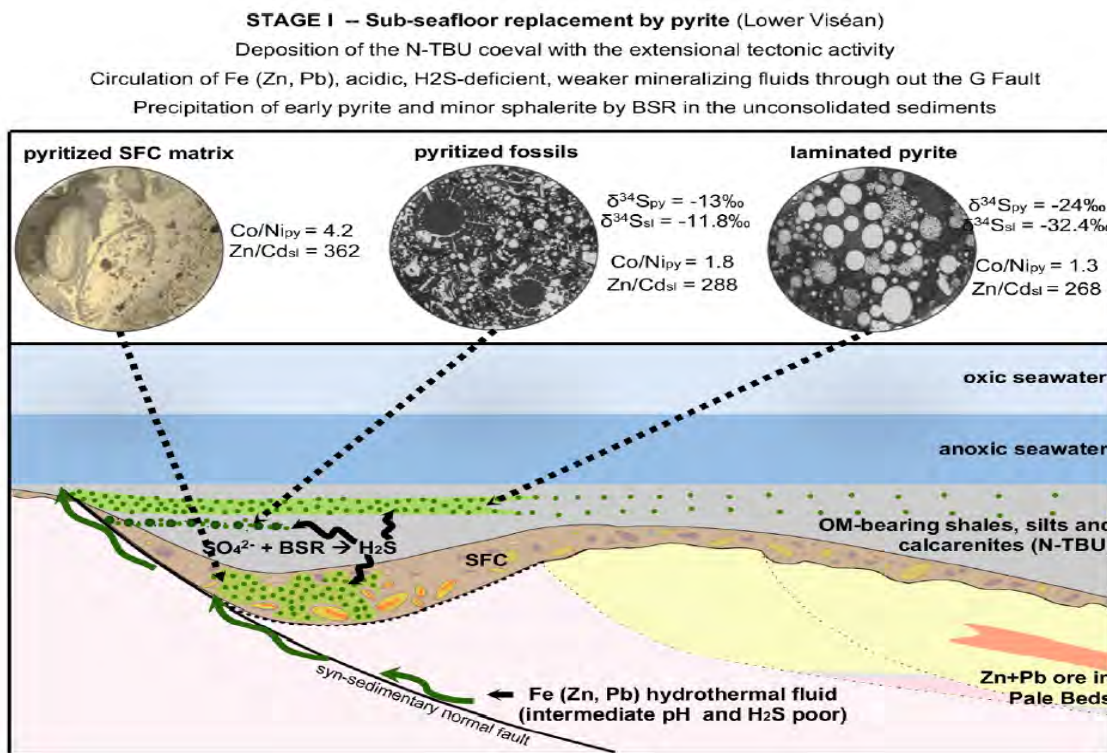
Figure 10. *Two-stage genetic model for the Tara Deep Lower Visean mineralization. Stage I - Sub-seafloor replacement by pyrite; and Stage II - Deposition of minor higher-temperature sulphide assemblages. OM = organic matter; BSR = Bacterial sulphate reduction.*

Howards Pass in the Yukon deposits (Hamilton *et al.*, 1982; Goodfellow, 2004; Gwosdz & Krebs, 1977; Turner *et al.,* 2000). These deposits include, in their outer margins, bedded hydrothermal products extending for up to several kilometres from the discharge zone. These distal facies include laminated pyrite, Mn enrichment, cherts, iron and calcium carbonates, iron oxides, barite and phosphates (Gwosdz & Krebs, 1977; Large, 1981; Hamilton *et al.*, 1982; S´aez *et al.*, 1999).

A potentially important observation is that the Tara Deep halo contains multiple episodes of mineralization recorded by veining, infilling, and replacement of bedded sulphides by typically higher-temperature assemblages (Fig. 4i-j, 6f-h, 7 g-i). These late assemblages share identical mineralogy and texture in matrix cementing the SFC and N-TBU (compare Fig. 4i with Fig. 7i), and in their S isotope values (Fig. 8), which in turn, matches with the late mineral association in the Pale Beds-hosted mineralization (see Figs. 5 and 7 of Yesares *et al.*, 2019).

Conclusions

Summary of mineralizing events

Assuming genetic models previously proposed for the Navan deposit, primary Zn + Pb sulphides hosted by the Pale Beds at Tara Deep formed by epigenetic replacement of carbonates where normal faults acted as pathways for ascending, relatively-warm, H_2S-poor, metal-bearing fluids. These mineralizing fluids scavenged metal from the underlying Lower Palaeozoic basement and then mixed with a cooler, hypersaline brine carrying SO_4.

The ongoing extensional tectonic activity in the area during the Lower Visean led to the erosion of parts of the early mineralized Pale Beds and the development of the SFC. The deposition of fault-talus sedimentary breccias which included reworked clasts of sulphide supports a Lower Visean minimum age for the onset of sulphide mineralization in the micrites.

Mineralizing events in the Lower Visean record at Tara Deep can be summarized in two stages (Fig. 10):

Stage I - Sub-seafloor replacement by pyrite

Acidic, H_2S-deficient, metal-exhausted and/or originally more dilute mineralizing fluids ascended to the SFC and N-TBU pile via the G Fault and possibly the S Fault. Fe-rich hydrothermal fluids circulated along the weakly oxic to anoxic diagenetic environment where metals were trapped in open spaces of the SFC, as well as organic material-bearing shales and calcarenites of the N-TBU. Fe and minor Zn were fixed by H2S produced by BSR, thereby precipitating a large amount of framboidal pyrite, together with associated sphalerite, and causing pyritization of fossils.

Stage II - Deposition of minor higher-temperature sulphide assemblages

Continued flow of metal-bearing fluids led to Fe-sulphide recrystallization and the replacement of earlier laminated pyrite and pyritized fossils by later higher temperature sulphides.

Evidence of soft-sediment deformation by both incoming stage II fluids (Fig. 6d) and by chert growth (Fig. 7a) suggests that there was no large time interval between stages I and II and that they possibly overlapped. Mineralogical, mineral chemistry and isotopic data for stage II sulphides indicate that the mineralizing fluids evolved to become more reduced, warmer and more acidic, perhaps due to deepening basement fluid circulation, enabling Cu, Co, Sb and Si transportation. The rapid cooling of metal-bearing fluids by interaction with the cooler sedimentary and diagenetic environment induced the precipitation of later sulphides in the matrix of the SFC, as well as replacive assemblages and hydrothermal cherts in the N-TBU. The lack of mineralization in higher stratigraphic levels implies that hydrothermal activity in the Tara Deep area ceased after deposition of hydrothermal chert at the top of the N-TBU.

A high degree of preservation of the SedEx halo (*i.e.*, framboids) indicates that organic-rich black shales provided reducing conditions which precluded sulphide oxidation. Moreover, later continuing thick sedimentation during formation of the Fingal Group has favoured the preservation of the original mineralization.

Implications for exploration

Economic and potentially economic Pale Beds-hosted Zn-Pb mineralization in the Navan area is widespread, distributed from the Main Navan Orebody to Tara Deep. However, there are no known deposits further to the southeast of Tara Deep. There is no a priori reason for the paucity of deposits, as the geodynamic extensional setting and host rocks are particularly favourable for mineralization. Although this southeastern area has yet to be subject to exploration drilling, analogous, more deeply buried, mineralization may be present. Thus, better understanding and definition of the sub-economic sulphide halos overlying the much higher-grade Tara Deep deposit provides valuable information for exploration and may enhance mineral exploration strategies for deeply buried deposits.

According to the results of the study, although hydrothermal products in both the N-TBU and SFC may extend a few kilometres, they are best developed close to normal faults and immediately above the underlying micrite-hosted mineralization, indicating pathways for ore-forming fluids and links between different mineralization styles.

At the deposit-scale, as discussed above, debris flows and sedimentary breccias are good evidence for *syn*-sedimentary faulting. Detailed studies on samples from a drill core at the southeast limit of Tara Deep indicate that there is more *syn*-sedimentary breccia in this area. Also, the presence of both laminated pyrite and minor high temperature sulphide assemblages in black shale samples in this area are a good indicator for possible presence of undiscovered deeper mineralization.

The apparent genetic linkage between sub-seafloor exhalative and underlying replacive mineralization in the Navan area may have geological and exploration implications for other sediment-hosted mineral provinces. Exhalative mineralization, including economic deposits, may represent halos of underlying replacive deposits, especially where carbonate footwall rocks are developed.

Declaration of Competing Interest

Acknowledgements

Appendix A. Supplementary data

Supplementary data to this article can be found online at https://doi. org/10.1016/j.oregeorev.2021.104415.

References

Adachi, M., Yamamoto, K., Sugisaki, R., (1986) Hydrothermal chert and associated siliceous rocks from the northern pacific: their geological significance as indication of ocean ridge activity: *Sediment. Geol.* v.47, 125–148.

Anderson, I.K. (1990) Ore depositional processes in the formation of the Navan zinc-lead deposit, Co. Meath, Ireland: Unpublished PhD Thesis, University of Strathclyde.

Anderson, I.K., Andrew, C.J., Ashton, J.H., Boyce, A.J., Caulfield, J.B.D., Fallick, A.E., Russell, M.J., (1989) Preliminary sulphur isotope data of diagenetic and vein sulphides in the Lower Palaeozoic strata of Ireland and southern Scotland: implications for Zn + Pb + Ba mineralization. *Journal of the Geological Society* v.146, 715–720.

Anderson, I.K., Ashton, J.H., Boyce, A.J., Fallick, A.E., Russell, M.J., (1998) Ore depositional processes in the Navan Zn-Pb deposit, Ireland. *Economic Geology and the Bulletin of the Society of Economic Geologists* v. 93, 535–563.

Andrew, C.J. (1993) Mineralization in the Irish Midlands, in Pattrick, R.A.D., and Polya, D.A. eds., *Mineralization in the British Isles,* Chapman & Hall, London, p. 208-269.

Andrew, C.J., & Ashton, J.H., (1985) The regional setting, geology and metal distribution patterns of the Navan orebody, Ireland: *Trans. Instn Min. Metall (Sect B: Appl. earth sci.)* v.94, 66–93.

Arthur M.A, & Sageman, B.B. (1994) Marine black shales: Depositional mechanisms and environments of ancient deposits: *Annual Review Earth and Planetary Sciences* v. 22 1994 499 551.

Ashton, J.H., Beach, I.A., Blakeman, R.J., Coller, D., Henry, P., Lee, R., Hitzman, M., Hope, C., Huleatt-James, S., O'Donovan, B., Philcox, M.E., (2018) Discovery of the Tara Deep Zn–Pb Mineralization at the Boliden Tara Mine. *SEG Special Publications*, *Society of Economic Geologists,* Littleton, CO, USA, Navan, Success with Modem Seismic Surveys, pp. 365–381.

Ashton, J.H., Blakeman, R.J., Geraghty, J.F., Beach, A., Coller, D., Philcox, M.E., (2015) The Giant Navan carbonate-hosted Zn–Pb deposit-A review. In: Archibald, S.M., Piercey, S.J. (Eds.), Current Perspectives on Zinc Deposits. I*rish Association for Economic Geology, Dublin, Ireland,* pp. 85–122.

Ashton, J.H., Downing, D.T., & Finlay, S., (1986) The geology of the Navan Zn–Pb orebody. In: Andrew, C.J., Crowe, R.W.A., Finlay, S., Pennell, W.M., Pyne, J.F. (Eds.), Geology and genesis of mineral deposits in Ireland. *Irish Association for Economic Geology, Dublin, Ireland*, pp. 243–280.

Ashton, J.H., Holdstock, M.P., Geraghty, J.F., O'Keeffe, W.G., Martinez, N., Peace, W., & Philcox, M.E., (2003) The Navan Orebody — discovery and geology of the South West Extension, in Kelly J.G, et al., (eds), Europe's Major Base Metal Deposits: *Irish Association for Economic Geology, Dublin,* p. 405–436.

Blakeman, R.J., Ashton, J.H., Boyce, A.J., Fallick, A.E., & Russell, M.J., (2002) Tirning of interplay between hydrothermal and surface fluids in the Navan Zn+Pb orebody, lreland: Evidence from metal distribution trends, mineral textures and δ34S analyses. *Economic Geology* v.97, 73–91.

Bond, D.P.G., & Wignall, P.B., (2010) Pyrite framboid study of marine Permian-Triassic bound-ary sections: a complex anoxic event and its relationship to contemporaneous mass extinction: *Geol. Soc. Am. Bull.* v.122, 1265–1279.

Boudreau, B.P., 1990. Asymptotic forms and solution of the model for silica-opal diagenesis in bioturbated sediments. *J. Geophys. Res.* v.95, 7367–7379.

Boyce, A.J., Anderton, R., & Russell, M.J., (1983) Rapid Subsidence and Early Carboniferous Base-Metal Mineralization In Ireland: *Trans. Instn Min. Metall. (Sect B: Appl. Earth Sci.)* v.92, 55–66.

Boyce, A.J., Fallick, A.E., Fletcher, T.J., Russell, M.J., & Ashton, J.H., (1994) Detailed Sulphur isotope studies of Lower Palaeozoic-hosted pyrite below the giant Navan Zn + Pb mine, Ireland: Evidence of transport of crustal S to a sediment-hosted deposit. *Mineralogical Magazine* v.58A, 109–110.

Boyce, A.J., Little, S.C., & Russell, M., (2003) A New Fossil Vent Biota in the Ballynoe Barite Deposit, Silvermines, Ireland: Evidence for Intracratonic Sea-Floor Hydrothermal Activity About 352 Ma. *Economic Geology* v. 98, 649–656.

Braithwaite, C.J.R., & Rizzi, G., (1997) The geometry and petrogenesis of hydrothermal dolomites at v. 44, 421–440.

Brimhall G.H., & Crerar, D.A.,)1987) Ore fluids: magmatic to supergene, in: Carmichael, I.S. E., Eugster, H.P., eds, Thermodynamics and modelling of geological materials: minerals, fluids and melts: *Reviews in mineralogy*, v. 17, p. 235–321.

Canfield, D.E., & Thamdrup, B., (1994) The production of 34S depleted sulfide during bacterial disproportionation of elemental sulfur. *Science* v.80 (266), 1973–1975.

Chen, Y.Q., Jiang, S.Y., Zhou, X.Y., Yang, W.J., & Han, L.J., (2010) δ30Si, δ18O and elements geochemistry on the bedded siliceous rocks and cherts in dolostones from Cambrian strata: Tarim Basin. *Geochimica* v.39 (2), 159–170.

Chowdhury, S., & Lentz, D.R., (2017) Minor- and trace-element characteristics of different pyrite types and their S-isotope 2 geochemistry from the Proterozoic Rakha Copper deposit. Singhbhum Shear Zone, India: *Journal of Mineralogy and Geochemistry* v.194 (3), 251–277.

Cooke, D., Bull, S., Large, R., & McGoldrick, P., (2000) The importance of oxidized brines for the formation of Australian Proterozoic stratiform sediment- hosted Pb-Zn (SEDEX) deposits. *Economic Geology* v.95, 1–18.

Derry, D.R., Clark, G.R., & Gillatt, N., (1965) The Northgate base-metal deposit at Tynagh, County Galway, Ireland: *Econ. Geol.* v.60, 1218–1237.

Eker, C.S., Sipahi, F., & Kaygusuz, A., (2012.) Trace and rare earth elements as indicators of provenance and depositional environments of Lias cherts in Gumushane, NE Turkey. Chemie der Erde – Geochem. – Interdiscip. *J. Chem. Problems Geosci. Geoecol* v. 72 (2), 167–177.

Emsbo, P., (2009) Geologic criteria for the assessment of sedimentary exhalative (sedex) Zn-Pb-Ag deposits: *U.S. Geol Surv Open-File Report* 1209, 21.

Everett, C.E., Rye, D.M., & Ellam, R.M., (2003) Source or sink? An assessment of the role of the Old Red Sandstone in the genesis of the Irish Zn–Pb deposits: *Econ. Geol.* v.98, 31–50.

Everett, C.E., & Wilkinson, J.J., (2001) Fluid Evolution at the Navan Deposit: Preliminary fluid inclusions results: Unpublished Report to Tara Mines Ltd., 14p.

Fallick, A.E., McConville, P., Boyce, A.J., Burgess, R., & Kelley, S.P., (1992) Laser microprobe stable isotope measurements on geological materials: Some experimental considerations (with special reference to 34S in sulphides): *Chem. Geol.* v.01, 53–61.

Fallick, A.E., Ashton, J.H., Boyce, A.J., Ellam, R.M., & Russell, M.J., (2001) Bacteria were responsible for the magnitude of the world-class hydrothermal base-metal orebody at Navan, Ireland: *Econ. Geol.* v.96, 885–890.

Fleischer, M., (1956) Minor Elements in Some Sulfide Minerals?: *Economic Geology,* v. 50th Anniversary, p. 970–1024.

Ford, C.V., (1996) The integration of petrologic and isotopic data from the Boulder Conglomerate determine the age of the Navan orebody Ire land: Unpublished Ph. D. thesis, University of Glasgow, p. 176. Fournier, 1985, The behavior of silica in hydrothermal systems, in: Geology and Geochemestry of Epithermal Systems: *Reviews: Economic Geology,* Berger, B.R., and Bethke, P.M., eds., v. 2, p. 45-61.

Fritschle, T., Daly, J.S., McConnell, B., Whitehouse, M.J., Menuge, J.F., Buhre, S., Mertz- Kraus, R., D¨opke, D., (2018) Peri-Gondwanan Ordovician arc magmatism in southeastern Ireland and the Isle of Man: Constraints on the timing of Caledonian deformation in Ganderia: *Geol. Soc. Am. Bull.* v.130, 1918–1939.

Gadd, M.G., Layton-Matthews, D., Peter, J.M., & Paradis, S.J., (2015) The world-class Howard's Pass SEDEX Zn-Pb district, Selwyn Basin, Yukon. Part I: trace element compositions of pyrite record input of hydrothermal, diagenetic, and metamorphic fluids to mineralization: *Miner. Depos.* v.1, 1–24.

Gagnevin, D., Boyce, A.J., Barrie, C.D., Menuge, J.F., & Blakeman, R.J., (2012) Zn, Fe and S isotope fractionation in a large hydrothermal system: *Geochim. et Cosmochim. Acta* v.88, 183–198.

Goodfellow, W.D., (1987) Anoxic stratified oceans as a source of sulphur in sediment-hosted stratiform ZnPb deposits (Selwyn Basin, Yukon, Canada): *Chemical Geology: Isotope Geoscience Section*, v. 65, p. 359–382.

Goodfellow, W.D., (2000) Anoxic conditions in the Aldridge Basin during formation of the Sullivan Zn-Pb deposit: implications for the genesis of massive sulphides and distal hydrothermal sediments. In: Lydon, J.W., Hoy, T., Slack, J.F., Knapp, M. (Eds.), The Geological Environment of the Sullivan Deposit, vol 1. *Mineral Deposits Division of the Geological Association of Canada, Special Publication, British Columbia*, pp. 218–250.

Goodfellow, W.D., (2004) Geology, genesis and exploration of SEDEX deposits, with emphasis on the Selwyn Basin. Narosa Publishing House, Canada, New Delhi, pp. 24–99.

Goodfellow, W.D., & Jonasson, I.R., (1984) Ocean stagnation and ventilation defined by 34S secular trends in pyrite and barite. Selwyn Basin, Yukon: *Geology* v.12, 583–586.

Goodfellow, W.D., & Lydon, J.W., (2007) Sedimentary exhalative (SEDEX) deposits, in Mineral Deposits of Canada, A Synthesis of Major Deposit Types, District Metallogeny, the Evolution of Geological Provinces, and Exploration Methods, Goodfellow, W.D., eds. *Special Publication v. 5 Geological Association of Canada, Mineral Deposits Division, St. John's, NL, Canada*, p. 163-183.

Goodfellow, W.D., Lydon, J.W., & Turner, R.J., (1993) Geology and genesis of stratiform sediment-hosted (SEDEX) zinc-lead-silver sulphide deposits: *Geological Association of Canada. Special Paper* 40, 201–252.

Gottesman, W., & Kampe, A., (2007) Zn/Cd ratios in calcsilicate-hosted sphalerite ores at Tumurtijn-Ovoo, Mongolia: *Geochim. Cosmochim. Acta* v.67, 323–328.

Gregory, D., Large, R.R., Halpin, J.A., Baturina, E.L., Lyons, T.W., Wu, S., Danyushevsky, L., Sack, P.J., Chappaz, A., Maslennikov, V.V., Bull, S.W., (2015) Trace element content of sedimentary pyrite in black shales: *Econ. Geol.* v.110, 1389–1410.

Gwosdz, W. & Krebs, W., (1977) Manganese halo surrounding Meggen ore deposit, Germany: *Institution of Mining and Metallurgy. Transactions, Section B, Applied Earth Science* v.86, 73–77.

Hamilton, J.M., Bishop, D.T., Morris, H.C., & Owens, O.E., (1982) Geology of the Sullivan orebody, Kimberley, B.C., Canada: Geological Association of Canada. Special Paper 25, 597–665. Han, Z.X., 1994. The Typomorphic characteristic of the sphalerite in the Qinling Devonian System lead–zinc metallogenic belt. *J. Xi'an College Geol.* v.16, 12–17.

Heaney, P.J., (1993) A proposed mechanism for the growth of chalcedony: *Contrib. Mineral. Petrol.* v115, 66–74.

Hemley, J.J., Cygan, G.L., Fein, J.B., Robinson, G.R., D'Angelo, W.M., (1992.) Hydrothermal ore-forming processes in the light of studies in rock buffered systems. Iron-copper-lead-zinc sulfide solubility relations: *Econ. Geol.* v87, 1–22.

Henkes, G.A., Passey, B.H., Grossman, E.L., Shenton, B.J., Yancey, T.E., Perez-Huerta, A., (2018) Temperature evolution and the oxygen isotope composition of Phanerozoic oceans from carbonate clumped isotope thermometry. *Geochimica et Cosmochimica Acta.* v490, 40–50.

Hitzman, M.W., Redmond, P.B., & Beaty, D.W., (2002) The carbonate-hosted Lisheen Zn–Pb- Ag deposits, County Tipperary, Ireland: *Econ. Geol.* v97, 1627–1655.

Hofmann, A., & Bolhar, R., (2007) Carbonaceous cherts in the Barberton Greenstone Belt and their significance for the study of early life in the Archean record. *Astrobiology* v7, 355–388.

Hopkinson, L., Roberts, S., Herrington, R., & Wilkinson, J., (1999) The nature of crystalline silica from the TAG submarine hydrothermal mound, 26◦ N Mid Atlantic Ridge: *Contrib. Mineral. Petrol.* v137, 342–350.

Johnson, C.A., Emsbo, P., Poole, F.G., Rye, R.O., (2009) Sulfur- and oxygen-isotopes in sediment-hosted stratiform barite deposits. *Geochimica et Cosmochimica Acta* v73, 133–147.

Kampschulte, A., Bruckschen, P., & Strauss, H., (2001) The sulphur isotopic composition of trace sulphates in Carboniferous brachiopods: implications for coeval seawater, correlation with other geochemical cycles and isotope stratigraphy: *Chem. Geol.* v175, 149–173.

Kaplan, I.R., Rittenberg, S.C., (1964) Microbiological Fractionation of Sulphur Isotopes. J. *Gen. Microbiol* v34, 195–212.

Kelley, K.D., & Jennings, S., (2004) A special issue devoted to barite and Zn-Pb-Ag deposits in the Red Dog district. Western Brooks Range, northern Alaska: Preface: *Economic Geology* v99, 1267–1280.

Kelley, S.P. & Fallick, A.E., (1990) High-precision, spatially resolved analysis of δ34S in sulfides using a laser extraction technique: *Geochim. et Cosmochim. Acta* v54, 883–888.

Kelley, S.P., Fallick, A.E., McConville, P., & Boyce, A.J., (1992) High precision, high spatial resolution analysis of sulfur isotopes by laser combustion of natural sulfide minerals. *Scanning Microsc.* v6, 129–138.

Lambert, I.B., & Scott, K.M., (1973) implications of geochemical investigations of sedimentary rocks within and around the McArthur zinc-lead-silver deposit. Northern Tenitoy: *Journal of Geochemical Exploration* v2, 307–330.

Large, D., & Walcher, E., (1999) The Rammelsberg massive sulphide Cu-Zn-Pb-Ba-deposit, Germany—An example of sediment-hosted, massive sulphide mineralization. *Mineralium Deposita* v34 (5–6), 522–538.

Large, R.R., Bodon, S., Davidson, G.J., Cooke, D.R., (1996) The chemistry of BHT ore formation-one of the keys to understanding the differences between SEDEX and BHT deposits: Hobart. University of Tasmania, CODES Special Publication 1, 105–111.

Large, R.R., & McGoldrick, P.J., (1998) Lithogeochemical halos and geochemical vectors to stratiform sediment-hosted Zn-Pb-Ag deposits, Part 1: Lady Loretta deposit, Queensland. *Journal of Geochemical Exploration* v63, 37–56.

Large, D.E., (1981) Geochemistry of sedimentary rocks in the vicinity of the Tom Pb-Zn- Ag deposit, Yukon Territory, Canada: 8th International Geochemical Exploration Symposium, Hanover, April 10–15, 1980. Transactions 203–217.

Large, R.R., Bull, S.V., McColdrick, P.J., (2000) Lithogeochemical halos and geocheinical vectors to stratiform sediment hosted Zn-Pb-Ag deposits. Part 2: HYC deposit. Northern Territory: Journal of Geochemical Exploration 64, 105–126.

Large, R.R., Bull, S.W., McGoldrick, P.J., Walters, S., Derrick, G.M., and Carr, G.R., (2005) Stratiform and strata-bound Zn-Pb-Ag deposits in Proterozoic sedimentary basins, northern Australia: *Economic Geology, 100th Anniversary Volume,* p. 931–963.

Large, R.R., Bull, S.W., Selley, D., Yang, J., Cooke, D., Garven, G., Mc- Goldrick, P., (2002) Northern Australian Proterozoic sediment-hosted Zn-Pb-Ag deposits: A summary: *Centre for Ore Deposit Research Special. Publication* v. 4, 159–160.

Large, R.R., Mukherjee, I., Gregory, D.D., Steadman, J.A., Maslennikov, V.V., (2017) Ocean and atmosphere geochemical proxies derived from trace elements in marine pyrite: implications for ore genesis in sedimentary basins. *Economic Geology* v112, 423–450.

Leach, D.L., Bradley, D.C., Huston, D., Pisarevsky, S.A., Taylor, R.D., Gardoll, J., (2010) Sediment-hosted lead-zinc deposits in Earth history. *Economic Geology* v105, 593–625.

Leach, D.L., Sangster, D.F., Kelley, K.D., Large, R.R., Garven, G., Allen, C.R., Gutzmer, J., &Walters, S., (2005) Sediment-hosted lead-zinc deposits: A global perspective: *Economic Geology, 100th Anniversary Volume,* p. 561–607.

Leeder, M.R., (1982) Upper Palaeozoic basins of the British Isles—Caledonide inheritance versus Hercynian plate margin processes. *J. Geol. Soc. Lond.* v139, 479–491.

Lei, Z., Dashtgardd, S.E., Wangc, J., Lie, M., Fenga, Q., Yuc, Q., Zhaoc, A., Duf, L., (2019) Origin of chert in Lower Silurian Longmaxi Formation: Implications for tectonic evolution of Yangtze Block, South China: Palaeogeography, Palaeoclimatology. *Palaeoecology.* v529, 53–66.

Li, S.R., Xu, H., & Shen, J.F., (2008) Crystallography and mineralogy: Geological Publishing Press. Beijing 1–181.

Liu, T.G., Ye, L., Zhou, J.X., Wang, X.L., (2010) Cd Primarily Isomorphously Replaces Fe but not Zn in Sphalerite: Acta Mineral. Sinica 30, 179–184.

Lydon, J.W., (1983) Chemical parameters controlling the origin and deposition of sediment-hosted stratiform lead-zinc deposits v. 9, 175–250.

Lydon, J.W., (1995) Sedimentary exhalative sulfides (SEDEX) in: Sinclair, O.R., Thorpe, W.D., Eckstrand, R.I. eds., Geology of Canadian mineral deposit types: *Geological Survey of Canada,* v. 8, p. 130–152.

Lydon, J.W., (2007) An overview of the economic and geological contexts of Canada's major mineral deposit types. In: Goodfellow, W.D. (Ed.), Mineral Deposits of Canada: A Synthesis of Major Deposit-types, District Metallogeny, the Evolution of Geological Provinces, and Exploration Methods, *Special Publication 5. Mineral Deposits Division, Geological Association of Canada*, pp. 3–48.

Lydon, J.W., Paakki, J., Anderson, H.E., & Reardon, N.C., (2000) An overview of the geology and geochemistry of the Sullivan Deposit, Chapter 27. In: Lydon, J.W., H¨oy, T., Slack, J.F., Knapp, M. (Eds.), The Geological Environment of the Sullivan Pb-Zn-Ag Deposit, v. 1. *Geological Association of Canada Mineral Deposits Division, Special Publication, British Columbia*, pp. 505–522.

Macaulay, C., Fallick, A., Haszeldine, R., & Graham, C., (2000) Methods of laser-based stable isotope measurement applied to diagenetic cements and hydrocarbon reservoir quality. *Clay Minerals* v (1), 313–322.

Maghfouri, S., Hosseinzadeh, M.R., Rajabi, A., Choulet, F., (2018) A review of major nonsulfide zinc deposits in Iran: *Geosci. Front*. v9 (1), 249–272.

Magnall, J.M., Gleeson, S.A., Blamey, N.J.F., Paradis, S., & Luo, Y., (2016) The thermal and chemical evolution of hydrothermal vent fluids in shale hosted massive sulphide (SHMS). In: systems from the MacMillan Pass district (Yukon, v. 193. *Geochimica et Cosmochimica Acta, Canada*), pp. 251–273.

Magnall, J.M., Gleeson, S.A., Creaser, R.A., Paradis, S., Glodny, J., Kyle, J.R., (2020) The mineralogical evolution of the clastic dominant (CD)-type Zn-Pb ± Ba deposits at Macmillan Pass (Yukon, Canada)—tracing subseafloor barite replacement in the layered mineralization. *Economic Geology* v115, 953–959.

Maliva, R.G., Knoll, A.H., & Simonson, B.M., (2005) Secular change in the Precambrian silica cycle: insights from chert petrology: *Geol. Soc. Am. Bull.* v117 (78), 835–845.

Marin-Carbonne, J., Chaussidon, M., & Robert, F., (2012) Micrometer-scale chemical and isotopic criteria (O and Si) on the origin and history of Precambrian cherts: implications for paleo-temperature reconstructions: *Geochim. Cosmochim. Acta* v92, 129–147.

Matsuhisa, Y., Goldschmidt, J.R. & Clayton, R.N., (1979) Oxygen isotopic fractionation in system quartz-albite-anorthite-water: Geochim. Cosmochim. Acta, 43, p. 1131 1140.

Miall, A.D., (2016) Stratigraphy: A Modern Synthesis: Springer International Publishing, p. 454.

Mills, H., Halliday, A.N., Ashton, J.H., Anderson, I.K., & Russell, M.J., (1987) Origin of a giant orebody at v. 327, 223–226.

Moroni, M., Naitza, S., Ruggieri, G., Aquino, A., Costagliola, P., De Giudici, G., Caruso, S., Ferrari, E., Fiorentini, M.E., Lattanzi, P., (2019) The Pb–Zn–Ag vein system at Montevecchio-Ingurtosu, southwestern Sardinia, Italy: A summary of previous knowledge and new mineralogical, fluid inclusion and isotopic d*ata: Ore Geol. Rev.* v115, 103194.

Movahednia, M., Rastada, E., Rajabib, A., Maghfouria, S., Gonz´alez, F.J., Alfonso, P., Choulete, F., Canetf, C., (2020) The Ab-Bagh Late Jurassic-Early Cretaceous sediment-hosted Zn-Pb deposit, Sanandaj-Sirjan zone of Iran: Ore geology, fluid inclusions and (S–Sr) isotopes. *Ore Geology Reviews* v121, 103484.

Mukherjee, I., & Large, R., (2017) Application of pyrite trace element chemistry to exploration for SEDEX style Zn-Pb deposits: McArthur Basin. Northern Territory, Australia: *Ore Geology Reviews* v81, 1249–1270.

Murowchick, J.B., & Barnes, H.L., (1986) Marcasite precipitation from hydrothermal solutions: Geochim. Cosmochim. Acta 50, 2615–2629. Ozsoy, E., Unluata, U., 1997. Oceanography of the Black Sea: a review of some recent results: *Earth. Sci. Rev.* v42, 231–272.

Peace, W.M., Wallace, W.M., Holdstock, M.P., & Ashton, J.H., (2003) Ore textures within the U lens of the Navan Zn-Pb deposit, Ireland. *Mineralium Deposita* v38, 568–584.

Peng, H.J., Mao, J.W., Hou, L., Shu, Q.H., Zhang, C.Q., Liu, H., & Zhou, Y.M., (2016) Stable isotope and fluid inclusion constraints on the source and evolution of ore fluids in the Hongniu-Hongshan Cu skarn deposit, Yunnan Province: China. *Econ. Geol.* v111, 1369–1396.

Philcox, M.E., (1984) Lower Carboniferous Lithostratigraphy of the Irish Midlands: *Irish Association for Economic Geology: Dublin, Ireland*, 89 p.

Philcox, M.E., (1989) The mid-Dinantian unconformity at Navan, Ireland, in: Arthurton R.S., Gutteridge, P. and Nolan, S.C., eds,. 'he role of tectonics in Devonian and Carboniferous sedimentation in the British Isles: *Yorkshire Geological Society, Occasional Publication*, v. 6, p. 67-8.

Phillips, W.E., & Sevastopulo, G.D., (1986) The structural and stratigraphic setting of Irish mineral deposits. In: Andrew, C.J., Crowe, R.W.A., Findlay, S., Pennell, W.M., Pyne, J.F. (Eds.), Geology and genesis of mineral deposits in Ireland. *Irish Association for Economic Geology, Dublin*, pp. 1–30.

Ramdohr, P., (1980) The Ore Minerals and their Intergrowths. v. 1 and 2. Pergamon, Oxford, 1207 p.

Rees, J.G., (1987) The Carboniferous Geology of the Boyne Valley area, Ireland: Unpublished PhD Thesis, Trinity College Dublin. Rees, J.G., 1992. The Courceyan (Lower Carboniferous) succession at Slane. County Meath: Irish Journal of Earth Sciences 11, 113–129.

Reed, M.H., & Palandri, J., (2006) Sulfide Mineral Precipitation from Hydrothermal Fluids: Reviews in Mineralogy & Geochemistry, v. 2006, p. 609-631.

Rieger, P., Magnall, J.M., Gleeson, S.A., Lilly, R., Rocholl, A., & Kusebauch, C., (2020) Sulfur Isotope Constraints on the Conditions of Pyrite Formation in the Paleoproterozoic Urquhart Shale Formation and George Fisher Zn-Pb-Ag Deposit. Northern Australia: *Economic Geology* v115 (5), 1003–1020.

Rizzi, G., (1993) The sedimentology and petrography of Lower Carboniferous limestones and dolomites; host rocks to the Navan zinc-lead deposit, Ireland: Unpublished PhD thesis, University of Glasgow.

Romano, M., (1980) The stratigraphy of the Ordovician rocks between Slane and Collon, Eastern Ireland: *Earth Sci. R. Dubl. Soc.* v3, 53–79.

S´aez, R., Moreno, C., Gonz´alez, F., & Almod´ovar, G.R., (2011). Black shales and massive sulfide deposits: causal or casual relationships? Insights from Rammelsberg, Tharsis, and Draa Sfar: *Mineral. Depos.* v46, 585–614.

S´aez, R., Pascual, E., Toscano, M., & Almod.var, G.R., (1999) The Iberian type of volcanosedimentary massive sulfide deposits: *Mineral. Deposita* v34, 549–570.

Sangster, D.F., (2018) Toward an integrated genetic model for vent-distal SEDEX deposits: *Miner. Deposita* v53, 509–527.

Seo, J.H., Guillong, M., & Heinrich, C.A., (2012) Separation of molybdenum and copper in porphyry deposits: the roles of sulfur, redox, and pH in ore mineral deposition at Bingham Canyon: *Econ. Geol.* v107, 333–356.

Seward, T.M., Williams-Jones, A.E., & Migdisov, A.A., (2014) The chemistry of metal transport and deposition by ore-forming hydrothermal fluids: *Treatise Geochem.*, p. 29–57.

Schieber, J., Southard, J.B., & Schimmelmann, A., (2010) Lenticular shale fabrics resulting from intermittent erosion of water-rich muds—interpreting the rock record in the light of recent flume experiments. *Journal of Sedimentary Research* v80, 119–128.

Sharp, Z.D., (1990) A laser-based microanalytical method for the in situ determination of oxygen iso tope ratios of silicates and oxides. *Geochim. Cosmochim. Acta* v.54, 1353–1357.

Slack, J.F., Kelley, K.D., Anderson, V.M., Clark, J.L., Ayuso, R.A., (2004) Multistage silicification and Fe-Tl-As-Sb-Ge-REE enrichment in the Red Dog Zn-Pb-Ag district, northern Alaska: Geochemistry, origin, and explo-ration applications. *Economic Geology* v99, 1481–1508.

Smith, L.B., Schieber, J., & Wilson, R.D., (2019) Shallow-water onlap model for the deposition of Devonian black shales in v. 47, 1–5.

Strogen, P., Jones, G.Ll., & Somerville, I., (1990) Stratigraphy and sedimentology of Lower Carboniferous (Dinantian) boreholes from West Co. Meath, Ireland: *Geological Journal* v25, 103–137.

Strogen, P., Somerville, I.D., Pickard, N.A.H., Jones, G.Ll &Fleming, M., (1996) Controls on ramp, platform and basinal sedimentation in the Dinanian of the Dublin Basin and Shannon Trough, Ireland., in: Strogen, P., Somerville, I.D., and Jones, G.L. l., eds., Recent Advances in Lower Carboniferous Geology: *Geological Society Special Publication*, v. 107, p. 263-279.

Sugitani, K., Yamamoto, K., Adachi, M., Kawabe, I., & Sugisaki, R., (1998) Archeancherts derived from chemical, biogenic and clastic sedimentation in a shallowrestricted basin: examples from the Gorge Creek Group in the Pilbara Block: *Sedimentology,* v. 45(6), p.1045–1062.

Taylor, K.G., Macquaker, J.H.S., (2000) Early diagenetic pyrite morphology in a mudstone-dominated succession: the Lower Jurassic Cleveland Ironstone Formation v. 131, 77–86.

Tice, M.M., & Lowe, D.R., (2006) The origin of carbonaceous matter in pre-3.0 Ga greenstone terrains: a review and new evidence from the 3.42 Ga Buck Reef Chert. *Earth-Sci. Rev.* v76 (34), 259–300.

Torremans, K., Kyne, R., Doyle, R., Guven, J.F., & Walsh, J.J., (2018) Controls on Metal Distributions at the Lisheen and Silvermines Deposits: Insights into Fluid Flow Pathways in Irish-Type Zn–Pb Deposits: *Econ. Geol.* v113, 1455–1477.

Turner, R.J.W., (1991) Jason stratiform Zn-Pb-barite deposit, Selwyn Basin, Canada (NTS105-O-1): geological setting, hydrothermal facies and genesis, in: Abbott, J.G., and Turner, R.J.W., eds., Mineral deposits of the northern Canadian Cordillera. *International Association On the Genesis of Ore Deposits, Field Trip 14: Guidebook*, p. 137–175.

Turner, R.J.W., Leitch, C.H.B., & Ross, K.V., (2000) District-scale alteration associated M., and Slack, J., eds., The geological environment of the Sullivan deposit, British Columbia: Geological Association of Canada, Mineral Deposits Division, Special Publication 1, p. 408–439.

Van den Boorn, S.H.J.M., Van Bergen, M.J., Nijman, W., & Vroon, P.Z., (2007) Dual role of seawater and hydrothermal fluids in Early Archean chert formation: evidence from silicon isotopes. *Geology* v35, 939–942.

Van den Boorn, S., Van Bergen, M.J., Vroon, P.Z., de Vries, S.T., & Nijman, W., (2010) Silicon isotope and trace element constraints on the origin of 3.5 Ga cherts: implications for early Archaean marine environments. *Geochim. Cosmochim. Acta.* 7v4 (3), 1077–1103.

Vaughan, A., (1991) The Lower Palaeozoic geology of the Iapetus Suture zone in eastern Ireland, PhD Thesis, Trinity College Dublin, 237p.

Vaughan, A., & Johnston, J.D., (1992) Structural constraints on closure geometry across the Iapetus suture in eastern Ireland. *Journal of the Geological Society of London* v149, 65–74.

Wagner, T., Boyce, A.J., & Fallick, A.E., (2002) Laser combustion analysis of δ34S of sulfosalt minerals: Determination of the fractionation systematics and some crystal-chemical considerations. *Geochimica et Cosmochimica Acta* v66, 2855–2863.

Walshaw, R.D., Menuge, J.F., & Tyrrell, S., (2006) Metal sources of the Navan carbonate-hosted base metal deposit, Ireland: Nd and Sr isotope evidence for deep hydrothermal convection: *Miner. Depos.* v41, 803–819.

Wilkin, R.T., Barnes, H.L., & Brantley, S.L., (1996) The size distribution of framboidal pyrite in modern sediments: An indicator of redox conditions: *Geochim. Cosmochim. Acta* v60, 3897–3912.

Wilkinson, J.J., (2010) A review of fluid inclusion constraints on mineralization in the Irish ore field and implications for the genesis of sediment-hosted Zn–Pb deposits: *Econ. Geol.* 1v05, 417–442.

Wilkinson, J.J., Eyre, S.L., & Boyce, A.J., (2005) Ore-forming processes in Irish-type carbonate-hosted Zn–Pb deposits: Evidence from mineralogy, chemistry, and isotopic composition of sulfides at the Lisheen mine: *Econ. Geol.* v100, 63–86.

Wilkinson, J.J., & Hitzman, M.W., (2015) The Irish Zn–Pb Orefield: The View from 2014, in: Current Perspectives on Zinc Deposits, Archibold, S.M., Piercey, S.J., eds., *Irish Association for Economic Geology: Dublin, Ireland*, p. 59–72.

Xu, G., (1998) Geochemistry of sulphide minerals at Dugald River. NW Queensland, with reference to ore genesis: Mineralogy and Petrology 63, 119–139. Yamamoto, K., 1987. Geochemical characteristics and depositional environments of cherts and associated rocks in the Franciscan and Shimanto Terranes: Sediment. Geol. 52, 65–108.

Yesares, L., Drummond, D.A., Hollis, S.P., Doran A.L., Menuge, J.F., Boyce, A.J., Blakeman, R.J., & Ashton, J.H., (2019) Coupling Mineralogy, Textures, Stable and Radiogenic Isotopes in Identifying Ore-Forming Processes in Irish-Type Carbonate- Hosted Zn–Pb Deposits: Minerals, v. 9(6), p. 335-362.

Zhai, Y.S., Yao, S.Z., & Cai, K.Q., (2011) Mineral Deposits, third ed. Geological Publishing House, Beijing (in Chinese).

Zhu, G.C., (1988) The typomorphic characteristics and genetic significance of main minerals in Baoshan Copper-Polymetal deposit: *Research Institute of Geology For Mineral Resources,* p. 56–63.